



1 **A SOUTH ATLANTIC ISLAND RECORD UNCOVERS SHIFTS IN**
2 **WESTERLIES AND HYDROCLIMATE DURING THE LAST GLACIAL**

3

4 **Svante Björck^{1,2}, Jesper Sjolte¹, Karl Ljung¹, Florian Adolphi^{1,3}, Roger Flower⁴, Rienk**
5 **H. Smittenberg², Malin E. Kylander², Thomas F. Stocker³, Sofia Holmgren¹, Hui Jiang⁵,**
6 **Raimund Muscheler¹, Yamoah K. K. Afrifa⁶, Jayne E. Rattray⁷, Nathalie Van der**
7 **Putten⁸**

8

9 ¹Department of Geology, Lund University, SE-22362 Lund, Sweden

10 ²Department of Geological Sciences and the Bolin Centre for Climate Research, Stockholm
11 University, SE-10691 Stockholm, Sweden

12 ³University of Bern, Physics Institute, Climate and Environmental Physics, Sidlerstrasse 5, CH-3012
13 Bern, Switzerland

14 ⁴Department of Geography, University College London, London WC1E 6BT, UK

15 ⁵Key Laboratory of Geographic Information Science, East China Normal University, 200062
16 Shanghai, PR China

17 ⁶School of Geography, Earth and Environmental Sciences, University of Birmingham, Edgbaston, B15
18 2TT, UK

19 ⁷Department of Biological Sciences, University of Calgary, Calgary, Canada

20 ⁸Earth and Climate Cluster, Faculty of Science, Vrije Universiteit, Amsterdam, The Netherlands

21

22 **Correspondence:** Svante Björck (svante.bjorck@geol.lu.se)

23 **Abstract**

24 The period 36-18 ka was a dynamic phase of the last glacial, with large climate shifts in both
25 hemispheres. Through the bipolar seesaw, the Antarctic Isotope Maxima and Greenland DO
26 events were part of a global “concert” of large scale climate changes. The interaction between
27 atmospheric processes and Atlantic meridional overturning circulation (AMOC) is crucial for
28 such shifts, controlling upwelling- and carbon cycle dynamics, and generating climate tipping
29 points. Here we report the first temperature and humidity record for the glacial period from
30 the central South Atlantic (SA). The presented data resolves ambiguities about atmospheric
31 circulation shifts during bipolar climate events recorded in polar ice cores. A unique lake
32 sediment sequence from Nightingale Island at 37°S in the SA, covering 36.4-18.6 ka, exhibits
33 continuous impact of the Southern Hemisphere Westerlies (SHW), recording shifts in their



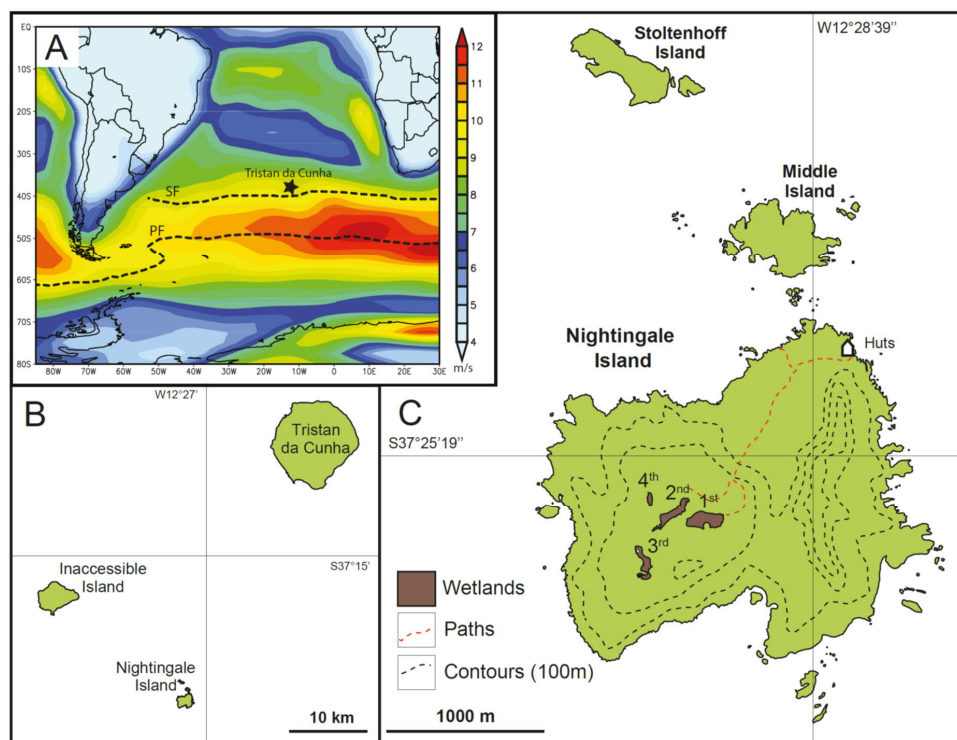
34 position and strength. The SHW displayed high latitudinal and strength-wise variability 36-31
35 ka locked to the bipolar seesaw, followed by 4 ka of slightly falling temperatures, decreasing
36 humidity and fairly southern westerlies. After 27.5 ka temperatures decreased 3-4°C, marking
37 the largest hydroclimate change with drier conditions and a variable SHW position. We note
38 that periods with more intense and southerly positioned SHW are correlated with periods of
39 increased CO₂ outgassing from the ocean. Changes in the cross-equatorial gradient during
40 large northern temperature changes appear as the driving mechanism for the SHW shifts.
41 Together with coeval shifts of the South Pacific westerlies, it shows that most of the Southern
42 Hemisphere experienced simultaneous atmospheric circulation changes during the latter part
43 of the last glacial.

44 **1 Introduction**

45 The Southern Hemisphere Westerlies (SHW) is a major determinant of hydroclimate in the
46 Southern Hemisphere (SH). In coupling marine and atmospheric processes, they are thought
47 to have played a pivotal and multi-faceted role during and at the end of the last ice age by
48 triggering changes in ocean-atmosphere CO₂ fluxes by physical processes (Saunders et al.,
49 2018; Toggweiler and Lea, 2010) and Fe fertilization of the Southern Ocean through varying
50 dust deposition (Lamy et al., 2014; Martin and Fitzwater, 1988; Martínez-García et al., 2014),
51 as well as regulating the salt and heat leakage from the Agulhas current to the Atlantic
52 meridional overturning circulation (AMOC) (Bard and Rickaby, 2009). In addition, changes
53 in AMOC, SHW strength and position, and Southern Ocean upwelling seem to have been
54 important mechanisms for different glacial CO₂ modes (Ahn and Brook, 2014). The position
55 of the SHW during glacial times is debated with some arguing for a northward displacement
56 (Toggweiler et al., 2006), while others argue for a southward move (Sime et al., 2013, 2016)
57 during the Last Glacial Maximum (LGM), relative to the present. Holocene data also suggest
58 an expanding-contracting SHW zone (Lamy et al., 2010). With these multiple scenarios the



59 pattern of SHW shifts and their detailed role for ocean ventilation and the global carbon cycle
60 remains unclear. It is postulated that the SHW moved in concert with rapid climate shifts
61 recorded in Greenland ice cores known as Dansgaard-Oeschger (DO) cycles (Markle et al.,
62 2016), and that these shifts are part of inter-hemispheric climate swings involving heat
63 exchange between the hemispheres through the atmosphere and the ocean, with atmospheric
64 heat fluxes partly compensating anomalous marine heat fluxes (Pedro et al., 2016). Whether
65 SHW zonal shifts only occurred in the Pacific sector of the Southern Ocean (Chiang et al.,
66 2014) or if they occurred throughout the SH is another crucial question (Ceppi et al., 2013).
67 Other key climate issues relate to the effects and areal extent of the bipolar seesaw mechanism
68 (Broecker, 1998; Stocker and Johnsen, 2003) and any signs of an early and long temperature
69 minimum at southern mid-latitudes matching Antarctic LGM (EPICA Community Members
70 et al., 2006). The lack of climate proxy records directly reflecting atmospheric conditions in
71 the central South Atlantic means that such information at these latitudes during the glacial are
72 primarily based on remote proxy records or climate model simulations. This results in a
73 largely unconstrained understanding of glacial conditions over vast parts of the mid-South
74 Atlantic, especially between 20-50°S where archives reflecting atmospheric processes are
75 absent.



76

77 **Figure 1.** (A) The position of the Tristan da Cunha island group in the South Atlantic, the 1000mb mean
78 annual wind speed (m/s) for 1980-2010 according to NCEP/NCAR reanalysis data indicating yellow-
79 red colors for the zone of the Southern Hemisphere Westerlies, and the positions of the Subtropical Front
80 (SF) and the Polar Front (PF) as dashed lines. (B) The three main islands of the Tristan da Cunha island
81 group. (C) The position and size of the four overgrown lake basins, so-called ponds (1P-4P), on
82 Nightingale Island with 100 m contour lines.

83

84 **2 Study site**

85 The Tristan da Cunha island group (TdC) at 37.1° S (Fig. 1) sits strategically at the northern
86 boundary of the SHW (Fig. 1A), a few degrees north of the Subtropical Front (SF), where sea
87 surface temperatures (SST) and salinities decrease by 3-4°C and 0.3 per mil, respectively.
88 Annual mean air temperature and precipitation are 14.3°C and approximately 1500 mm,
89 respectively, with highest precipitation in austral winter when the SHW impact is largest. The
90 record presented here is from 1st Pond (1P), an overgrown crater lake (200x70 m, 207 m a.s.l.)



91 in the central part of Nightingale Island (NI) (Fig. 1C and Fig. 2), a volcanic island dominated
92 by trachytic bedrock. Its drainage area is about twice the size of today's peat-bog and is thus
93 sensitive to changes in the precipitation/evaporation balance (P/E). Previous studies from NI
94 show that the area experienced shifts in precipitation during the Holocene (Ljung and Björck,
95 2007) and partly also during the Last Termination (Ljung et al., 2015), mainly attributed to the
96 changing impact of the SHW. These data also indicate a southerly displacement of the
97 Intertropical Convergence Zone (ITCZ) during the Heinrich 1 event (H1), and warming in the
98 South Atlantic as a consequence of reduced AMOC, causing the lake basin to dry out, creating
99 a hiatus between 18.6-16.2 ka (Ljung et al., 2015). Here we present a multi-proxy study of the
100 sediments that accumulated before this hiatus dating to 36.4-18.6 ka, covering the younger
101 part of Marine Isotope Stage 3 (MIS 3) and most of MIS 2, a climatically very dynamic
102 period with Antarctic Isotope Maxima, DO and H events. In spite of its fairly northern
103 position in relation to Antarctica we hypothesize that TdC was impacted by such events in
104 terms of shifts of SHW, which we aim to test by using a suite of proxies.



105

106 **Figure 2.** Photograph from Nightingale Island. The over-grown lake basins of 1st and 2nd Pond are
107 shown, with the higher situated 1st Pond in the background, seen towards southeast. Note the albatross
108 chicks (white dots) and the four persons on 2nd Pond as scale. Photo S. Björck.

109 **3 Material and methods**

110 **3.1 Field work, handling of cores and sample collection**

111 Two weeks of field work on NI were carried out in February 2010 and drilling was carried out
112 using Russian chamber samplers providing 1 m long cores ($\varnothing=50$ and 75 mm) with overlaps
113 of 15-50 cm between each cored section. The ketch *Ocean Tramp* provided the transport from
114 the Falkland Islands to TdC and back to Uruguay. In order to penetrate as deep as possible



115 into the very stiff sediments a chain-hoist was used for coring the deeper parts of the
116 sequences. The sediments were described immediately in the field before being wrapped in
117 plastic film and PVC tubes. Upon arrival in Uruguay the cores were transported to the
118 Geology Department in Lund where they were stored in a cold room. Before sub-sampling for
119 the different proxy analyzes, the field-based lithostratigraphy and correlations between
120 individual core sections were adjusted in the laboratory. This was aided by magnetic
121 susceptibility (κ) measurements, which give a relative estimate of the magnetic mineral
122 concentration, to confirm and adjust the visual correlation between overlapping core
123 segments.

124

125 **3.2 Radiocarbon dating and age model**

126 The radiocarbon dated material consisted of 1 cm thick, organic-rich, bulk sediment. All 41
127 dated samples were pre-treated and measured at the Lund University Radiocarbon Dating
128 Laboratory with Single Stage Accelerator Mass Spectrometry (SSAMS). The age model was
129 constructed using the OxCal software package (Bronk Ramsey, 1995, 2009a). To minimize
130 subjective user input we ran the age model with a general outlier model (Bronk Ramsey,
131 2009b), and a variable k-value that lets the model itself determine the sedimentation rate
132 variability (Fig. 3). For calibration we use the Southern Hemisphere calibration dataset,
133 SHCal13 (Hogg et al., 2013)).

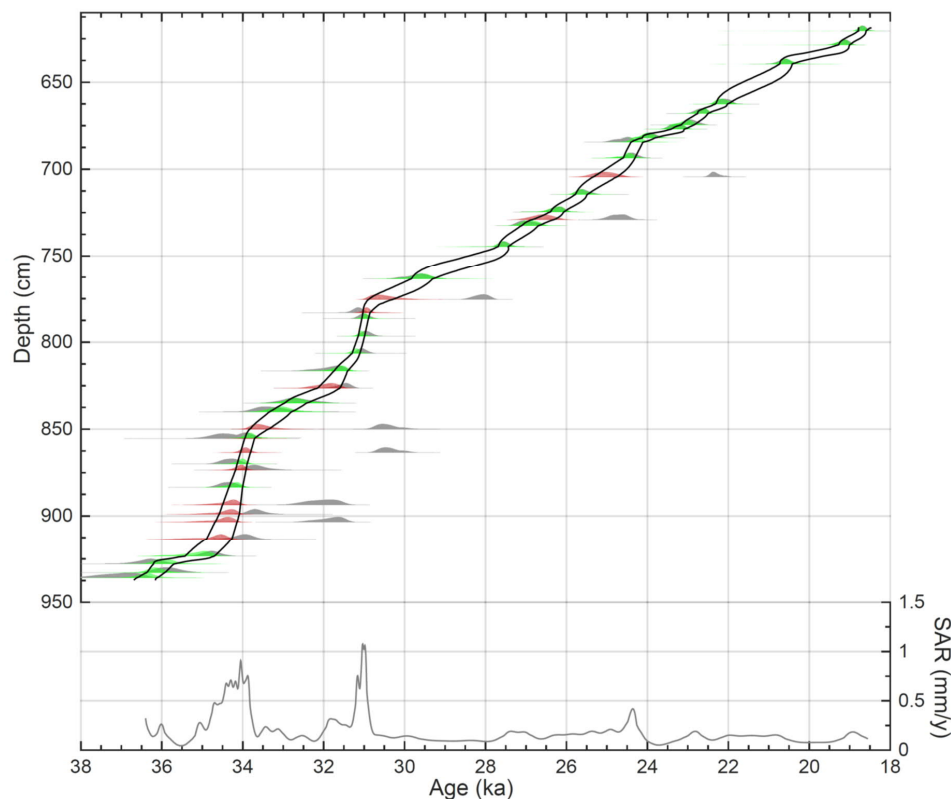
134

135 **3.3 Measurements for magnetic susceptibility**

136 Magnetic susceptibility (κ) was measured using a Bartington MS2E1 high resolution surface
137 scanning sensor coupled to a TAMISCAN automatic logging conveyor. Measurements were
138 carried out on non-sampled half cores and with a resolution of 5 mm and with results shown



139 in 10^{-6} SI units. The magnetic susceptibility gives a relative estimate of the ability of the
140 material to be magnetized, i.e. the magnetic mineral concentration.



141

142 **Figure 3.** Age model for the sediments at 1st Pond, Nightingale Island. Top panel: Radiocarbon based
143 age-depth model (black lines encompass the 68.2% probability interval). The patches indicate the
144 calibrated probability distributions of each radiocarbon date for un-modelled (single) dates (grey patch),
145 and their posterior distributions when modeled as a P-sequence: Green patches indicate agreement
146 indices of >60% and red patches agreement indices of <60%, i.e., outliers. Bottom panel: Sediment
147 accumulation rates (mm a^{-1}) based on the mean age-depth model shown in the top panel.

148

149 3. 4 XRF analyses

150 A handheld Thermo Scientific portable XRF analyzer (h-XRF) Niton XL3t 970 GOLDD+ set
151 in the Cu/Zn mining calibration mode was used. The instrumentation provides highly accurate
152 determinations for major elements (Helfert et al., 2011). All analyses were performed on
153 freeze-dried sediments from the 1P cores using an 8 mm radius spot size in order to obtain



154 representative values. The elemental detection depends partly on the duration of the analysis
155 at each point; this is especially true for the lighter elements such as Mg, Al, Si, P, S, Cl, K and
156 Ca. For this reason the measurement time of each sample was set to 6 minutes. Although a
157 larger suite of elements was acquired, we have chosen to work with Al, Si, P, S, K, Ca, Ti,
158 Mn, Fe, Rb, Sr and Zr. These elements were selected based on their analytical quality (i.e.,
159 level above the detection limit) and with the help of Principal Component Analysis (PCA).
160 PCA was made using JMP 10.0.0 software in correlation mode using a Varimax rotation.
161 Before analysis all data were converted to Z-scores calculated as $(X_i - X_{avg})/X_{std}$, where X_i is
162 the normalized elemental peak areas and X_{avg} and X_{std} are the series average and standard
163 deviation, respectively, of the variable X_i . A Varimax rotation allocates into the components
164 variables which are highly correlated (sharing a large proportion of their variance) – imposing
165 some constrains in defining the eigenvectors. By grouping together elements showing similar
166 variation, the chemical signals tend to be clearer and key elements are better identified. To
167 simplify the interpretation of our principal components (PC) we employ a modified Chemical
168 Index of Alteration (CIA), see Fig. 4D, as defined by Nesbitt and Young (1982): CIA =
169 $[Al_2O_3/(Al_2O_3 + CaO + NaO + K_2O)] \times 100$. This index expresses the relative proportion of
170 Al_2O_3 to the more labile oxides and is an expression of the degradation of feldspars to clay
171 minerals. Since we have no NaO data we call it a *modified CIA*.

172 **3.5 C and N analyses**

173 Dried and homogenized samples every 1-2 cm were analysed with a Costech Instruments ECS
174 4010 elemental analyzer. The accuracy of the measurements is better than $\pm 5\%$ of the
175 reported values based on replicated standard samples. C/N atomic ratios were obtained by
176 multiplying by 1.167.



177 **3.6 ¹³C and ¹⁵N analyses**

178 Dried homogenized bulk samples were measured using a ThermoFisher DeltaV ion ratio mass
179 spectrometer. The isotopic composition of samples is reported as conventional δ -values in
180 parts per thousand relative to the Vienna Pee Dee Belemnite (¹³C) and atmospheric N (¹⁵N):
181 $\delta_{\text{sample}} (\text{‰}) = [(R_{\text{sample}} - R_{\text{standard}}) / (R_{\text{standard}})] \times 1000$ where R is the abundance ratio of ¹³C/¹²C in
182 the sample or in the standard.

183 **3.7 Pollen analyses**

184 Sixty-four levels were sub-sampled and analysed for their pollen content. Pollen samples of 1
185 cm³ were processed following standard method A as described by Berglund and Ralska-
186 Jasiewiczowa (1986) with added *Lycopodium* spores for determination of pollen concentration
187 values. Counting was made under a light microscope at magnifications of x400 and x1000.
188 The aim was to count at least 500 pollen grains in every sample, which was almost achieved
189 (mean sum of 565 pollen grains and mean sum of 870 pollen grains and spores). Identification
190 of pollen grains and spores was facilitated by published photos (Hafsten, 1960), standard
191 pollen keys (Moore et al., 1991) and a small collection of type slides from Tristan da Cunha
192 borrowed from The National History Museum in Bergen. The pollen percentage diagram (Fig.
193 5) was plotted in C2 (Juggins, 2007). Warm/cold pollen ratios were calculated as $W_p / (W_p +$
194 $C_p)$, where warm pollen types (W_p) are from plants only found below 500 m a.s.l. and cold
195 pollen types (C_p) are from plants only found above 500 m a.s.l.

196 **3.8 Diatom analyses and diatom environmental ratios**

197 179 levels of 0.5 cm thick sediment segments were sub-sampled to analyse their diatom
198 content. For preparation of diatom slides ~ 200 mg freeze-dried sediment was oxidized with
199 15% H₂O₂ for 24 hours, then 30% H₂O₂ for a minimum of 24 hours, and finally heated at
200 90°C for several hours. A known quantity of DVB (divinylbenzene) microspheres was added
201 to 200 μ L aliquots of the digested and cleaned slurries in order to estimate diatom
202 concentrations (Battarbee and Keen, 1982). The diatoms were mounted in Naphrax® medium



203 (refractive index = 1.65). 300 valves or more per sample were counted in most samples and
204 identified largely using published diatom floras (Krammer and Lange-Bertalot, 1986; Lange-
205 Bertalot, 1995; Le Cohu and Maillard, 1983; Moser et al., 1995; Van de Vijver et al., 2002).
206 Diatom results are expressed as relative % abundance of each taxon (Fig. S3) and also as total
207 concentrations of valves per g dry sediment.

208 Freshwater diatom species are excellent indicators of water quality, particularly
209 of pH, conductivity and dissolved nutrients (Battarbee et al., 2001). Sedimentary diatom
210 assemblages *inter alia* can be used to reconstruct past changes in water quality using the
211 ecological indicator information for each species. Where suitable modern diatom–water
212 quality calibration data sets exist transfer functions can be generated to reconstruct these
213 changes. However, in sediment records where diatom diversity is low and affinities of some
214 species are not firmly established, placing diatom taxa into ecological/environmental
215 preference groups using literature attributions and field experience can be used to generate
216 ratio scores relevant to past conditions. The 1st Pond assemblages are suitable for such an
217 approach, particularly for inferring changes in habitat and water acidity. The acid diatom
218 index ratio is derived from the sum of acid water indicating taxa comprising *Aulacoseira*,
219 *Frustulia*, *Pinnularia* and *Eunotia* compared to that of the fragilarioid tychoplanktonic taxa.
220 Proportions of acidity tolerant to acidity intolerant diatom taxa indicate water pH, total
221 tychoplankton (temporary phytoplankton) vs. total benthic taxa relate to open water
222 conditions, subaerial/terrestrial taxa vs. the total assemblage indicate wetland development
223 and/or in-washed material.

224 **3.9 Biogenic silica analyses**

225 The 310 samples were analyzed using a wet-alkaline digestion technique (Conley and
226 Schelske, 2001). Samples were freeze-dried and gently ground prior to analysis.
227 Approximately 30 mg of sample was digested in 40 ml of a weak base (0.47M Na₂CO₃) at



228 85°C for a total duration of 3 hours. Subsamples of 1 ml were removed after 3 hours and
229 neutralized with 9 ml of 0.021 M HCl. Dissolved Si concentrations were measured with a
230 continuous flow analyzer applying the automated Molybdate Blue Method (Grasshoff et al.,
231 1983). Biogenic silica content in lake sediments is a proxy for lake productivity.

232 **3.10 Lipid biomarker and compound specific hydrogen isotopic analyses**

233 The hydrogen isotopic composition (δ notation) of *n*-alkanes was analyzed by gas
234 chromatography–isotope ratio monitoring–mass spectrometry (GC-IRMS) using a Thermo
235 Finnigan Delta V mass spectrometer interfaced with a Thermo Trace GC 2000 using a GC
236 Isolink II and Conflo IV system. Helium was used as a carrier gas at constant flow mode and
237 the compounds separated on a Zebtron ZB-5HT Inferno GC column (30 m x 0.25 mm x
238 0.25 μ m). Lipid extraction was performed on freeze-dried samples by sonication with a
239 mixture of dichloromethane and methanol (DCM-MeOH 9:1 v/v) for 20 minutes and
240 subsequent centrifugation. The process was repeated three times and supernatants were
241 combined. Aliphatic hydrocarbon fractions were isolated from the total lipid extract using
242 silica gel columns (5% deactivated) that were first eluted with pure hexane (F1) and
243 subsequently with a mixture of DCM-MeOH (1:1 v/v) to obtain a polar fraction (F2). A
244 saturated hydrocarbon fraction was obtained by eluting the F1 fraction through 10% AgNO₃-
245 SiO₂ silica gel using pure hexane as eluent. The saturated hydrocarbon fractions were
246 analyzed by gas chromatography – mass spectrometry for identification and quantification,
247 using a Shimadzu GCMS-QP2010 Ultra. C₂₁ to C₃₃ *n*-alkanes were identified based on mass
248 spectra from the literature and retention times. The concentrations of individual compounds
249 were determined using a calibration curve made using mixtures of C₂₁-C₄₀ alkanes of known
250 concentration. More details about the GC-IRMS method, including GC oven temperature
251 program, instrument performance and reference gases used, are given in Yamoah et al. (2016).
252 The average standard deviation for δ D values was 5%. Due to low sea levels during the time



253 period of our proxies the δD values of the *n*-alkanes were ice volume corrected (Tierney and
254 deMenocal, 2013), $\delta D_{\text{corr}} = (\delta D_{\text{wax}} + 1000) / (\delta O_{\text{w}}^{18} * 8 * 0.001 + 1) - 1000$, with interpolated ocean
255 water δO_{w}^{18} values (Waelbroeck et al., 2002).

256 Isoprenoid and branched glycerol dialkal glycerol tetraethers (GDGTs) were
257 measured on the F2 fractions after filtration through 0.45 μm PTFE filters and reconstitution
258 into a known volume of methanol. Analysis was done using a Thermo-Dionex HPLC
259 connected to a Thermo Scientific TSQ quantum access triple quadrupole mass spectrometer,
260 using an APCI interface. Chromatographic separation was achieved using a reverse phase
261 method similar to the one used by Zhu et al. (2013). Partially co-eluting GDGT isomers were
262 integrated as one peak in order to obtain data comparable to the normal phase method that has
263 been in use by the community since Weijers et al. (2007).

264 One prerequisite for the valid use of brGDGTs is a relatively high branched-
265 over-isoprenoid tetraether (BIT) index, which was 1.00 throughout the core. Reconstructed
266 pH values, based on the CBT ratio (Weijers et al., 2007) were stable at 6.6 ± 0.1 over the
267 length of the core, which means that temperature is the dominant environmental factor exerted
268 on the brGDGT distribution. At the time of measurement, we had not adopted the new method
269 which separates between 5-methyl and 6-methyl branched GDGTs (De Jonge et al., 2014). As
270 a consequence, we do not have individual quantifications of 5-methyl and 6-methyl branched
271 GDGT isomers needed to use the revised $\text{MBT}_{5\text{me}}$ temperature proxy for mineral soils (De
272 Jonge et al., 2014) or peat (Naafs et al., 2017), which gives lower RMSE than the original
273 terrestrial (soil) calibration (Weijers et al., 2007). However, since our data are from lake
274 sediments, we argue that GDGT-based temperature proxy calibrations based on lake surveys
275 is a valid approach. Indeed, using the original temperature calibration of Weijers et al. (2007)
276 resulted in very low temperatures between 0 and 6°C, a cold bias observed in other studies
277 from lakes. This bias is probably due to the addition of *in situ* produced brGDGTs on top of



278 any brGDGTs eroded from land (Loomis et al., 2012; Pearson et al., 2011). We therefore used
279 the global calibration of Pearson et al. (2011), based on a global lacustrine data set and using
280 mean summer temperatures, including samples from South Georgia Island in the S. Atlantic.
281 In addition, we also use a calibration based on a large data set of East African lakes from
282 different altitudes (Loomis et al., 2012), using mean annual temperatures, and which is also
283 applicable outside of East Africa (Loomis et al., 2012).

284 **3.11 Calculation of insolation values**

285 A long term numerical solution for Earth's insolation quantities (Laskar et al., 2004) was used
286 for the insolation values, 37-18 ka at 37°S, and calculated with the Analyseries program.
287 While the austral winter values (W/m²) were based on mean daily June-August insolation
288 (W/m²), the mean austral summer values were based on the mean daily December-
289 February insolation.

290 **3.12 Isotope model simulation**

291 The isotope model analysis is based on a 1200-year simulation using the isotope enabled
292 version of the ECHAM5/MPIOM earth system model (Werner et al., 2016) run with natural
293 and anthropogenic forcings for 800 to 2000 CE (Sjolte et al., 2018). Horizontal resolution of
294 the atmosphere is 3.75° x 3.75° (T31) with 19 vertical layers, while the ocean has a horizontal
295 resolution of 3° x 1.8° with 40 vertical layers. Since both the present day situation and our
296 Nightingale Island record show a continuous impact from the westerlies we deem it valid to
297 use this late Holocene simulation as an analogue for interpreting the variability of the
298 westerlies during the time period of study. The outcome of the simulation is presented in the
299 result section, but further investigation of the model run shows that the multi-decadal
300 variability of δD at TdC is related to the phase of the Antarctic Annular Mode, indicating that
301 isotopic variability at TdC is sensitive to large scale SH climate variability (Fig. S4).

302



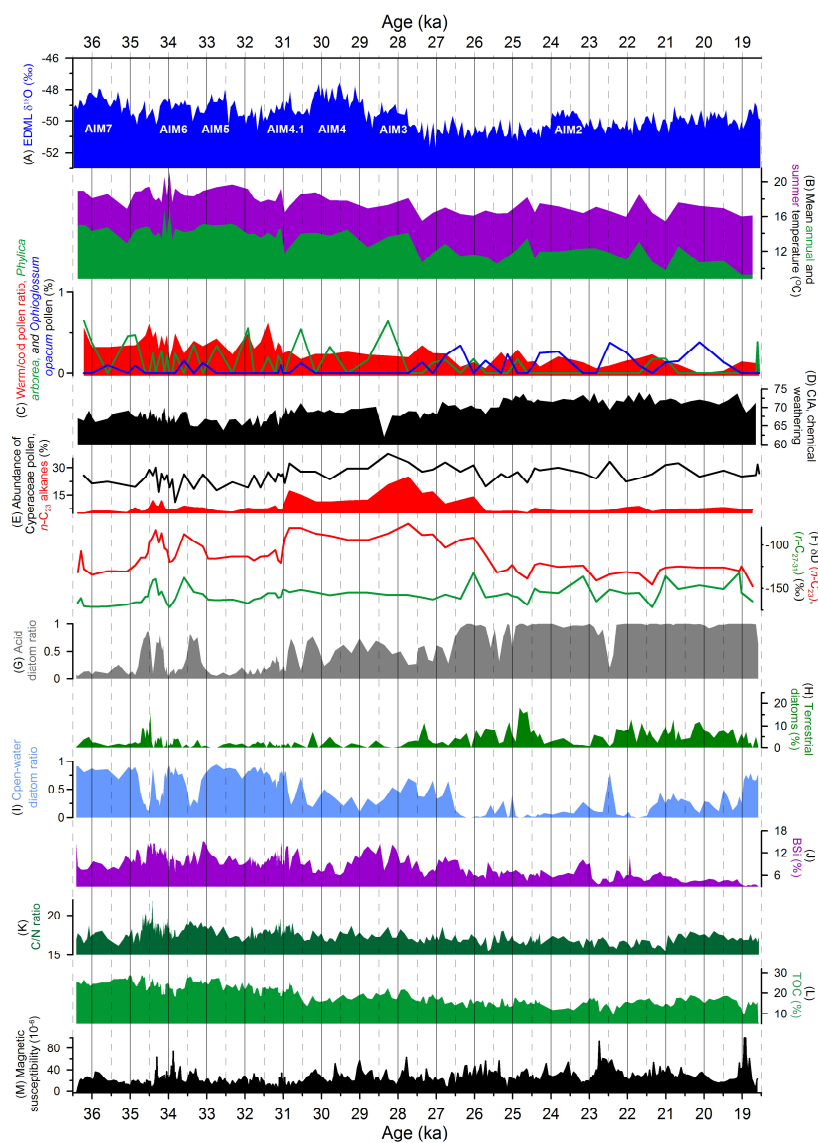
303 **3.13 Principal component analysis (PCA)**

304 PCA was performed with 14-16 of our variables (proxies) that we expect to respond to
305 hydroclimate changes, using the C2 program (Juggins, 2007). The aim was to display the
306 impact of different combination of proxies on samples in a biplot. Our two temperature
307 proxies MAT and the MST/MAT ratio were both included and excluded in the analyses and
308 this resulted in almost identical bi-plots in terms of positions of the variables. When the
309 temperature proxies are excluded PC1 is slightly weaker (38.1 vs 40.9%) while PC2 is
310 slightly stronger (13.4 vs 11.8%) than when they are included. We therefore include the
311 temperature proxies in our PCA to illustrate temperature together with the other proxies. All
312 the variables were centered and standardized before calculation.

313 **4. Results**

314 **4. 1 An island record of glacial climate in central South Atlantic**

315 Thirty-nine 1 m long overlapping cores were taken in February 2010 from three over-grown
316 crater lakes (Fig. 1C) between lava ridges (Anker Björk et al., 2011). 1P was exceptional in
317 that it was the only site where sediments older than 18.6 ka were recovered. At 1P the 16.2-
318 18.6 ka hiatus (Ljung et al., 2015) is marked by a thin silt lamina at 618.8 cm. We retrieved
319 five overlapping cores below the hiatus with 318.2 cm of sediments before coring was
320 obstructed at 937 cm by suspected bedrock or boulders. These cores were correlated by
321 lithology and magnetic susceptibility (MS). The lower 162 cm consist of a dark brown
322 slightly silty gyttja, overlain by a grey brown silty clay gyttja, all deposited under anaerobic
323 conditions. Because of the low concentration of plant macro-fossil remains our chronology is
324 based on 41 ¹⁴C dates of 1 cm thick bulk sediment samples between 620 and 936 cm (Table
325 S1). Comparisons of ¹⁴C dates of bulk sediment and plant remains (wood and peat) have
326



327

328 **Figure 4.** Antarctic ice core data and some of the proxy data from the sediments in 1st Pond, between
 329 36.4 and 18.6 ka. (A) The EDML $\delta^{18}\text{O}$ record (EPICA Community Members, 2006) showing AIM 7-2.
 330 (B) Mean annual and summer temperature from the GDGT analyses and calibrated with Pearson et al.
 331 (2011) and Loomis et al. (2012), respectively. (C) Warm pollen ratios, % *P. arborea* pollen and %
 332 *Ophioglossum* spores. (D) Modified chemical index of alteration (CIA). (E) % Cyperaceae pollen and
 333 *n*-C₂₃ alkanes. (F) δD values (‰) of *n*-C₂₃ and *n*-C₂₇₋₃₁ alkanes. (G) Acid diatom ratios. (H) % terrestrial
 334 diatoms. (I) Open water diatom ratios. (J) % biogenic silica (BSi). (K). C/N ratios. (L) % total organic
 335 carbon (TOC). (M) Magnetic susceptibility (MS) expressed as 10^{-6} SI units. All proxies are related to
 336 the age scale on the x-axes.



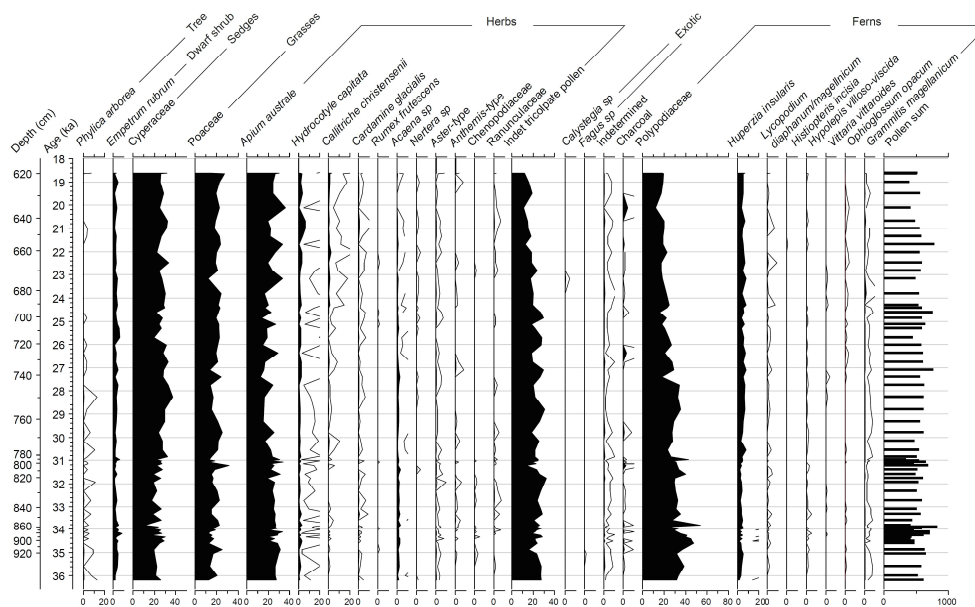
337 shown good concordance (Ljung et al., 2015; Ljung and Björck, 2007). Our age model (Fig.
338 3) displays a mean sedimentation rate of 0.18 mm yr^{-1} , but with considerable variation.

339 A large set of proxy data from 1P (Figs. 4-5, Figs. S1-S3, Table S2) was
340 analyzed and provides information about local changes such as soil conditions/erosion,
341 weathering, vegetation composition, organic productivity, lake conditions and P/E ratios.
342 Other proxies (GDGTs) display regional changes in temperature such as mean annual (MAT)
343 and mean summer temperatures (MST) and hydroclimate conditions (deuterium isotopes),
344 such as the source water of terrestrial and aquatic plants including evaporative conditions.
345 Principal component analysis (PCA) was performed to investigate co-variability between
346 proxies, showing the interplay of changes in hydroclimate driven by oceanic and atmospheric
347 circulation changes (Fig. 6).

348 In agreement with the supposed minimum age of pond formation through
349 volcanic activity (Anker Björk et al., 2011), the bottom of 1P has an age of $36.4 \pm 0.3 \text{ ka}$. Our
350 temperature records (Fig. 4B) show an oscillating pattern, with the largest change at 27.5 ka,
351 and share many similarities with the EDML curve (Fig. 4A). Before 27.5 ka MAT and MST
352 vary between $17\text{-}12^\circ\text{C}$ and $21\text{-}17^\circ\text{C}$, respectively, while the variation is between $13\text{-}9^\circ\text{C}$ and
353 $18.5\text{-}15.5^\circ\text{C}$, respectively, after 27.5 ka. In terms of pollen as a local temperature indicator it
354 is known that *Phyllica arborea*, *Acaena sarmentosa* and two Asteracea plant types are
355 sensitive to cold conditions (Ryan, 2007). They make up warm pollen types at NI and the
356 warm/cold pollen-types ratio (Fig. 4C) shows large variations until 31.4 ka, followed by a
357 two-step decline largely in contrast to the spore abundance of the cold tolerant *Ophioglossum*
358 *opacum* fern, and with a trend similar to the temperature curves. In comparison to Holocene
359 sediments from NI (Ljung and Björck, 2007), the glacial pollen record from 1P (Fig. 5) shows
360 less variability, and the most distinct difference is the very low abundance of the only tree
361 species pollen on the island, the frost limited *P. arborea*. Based on lapse rates, with 65-130 m



362 lower sea levels 35-18 ka (Lambeck et al., 2014), and today's distribution of *P. arborea* on
363 TdC and Gough Island (Ryan, 2007) we can estimate that its absence after 28 ka implies
364 minimum winter temperatures at least 3°C lower than today, which agrees well with our MAT
365 curve (Fig. 3B).



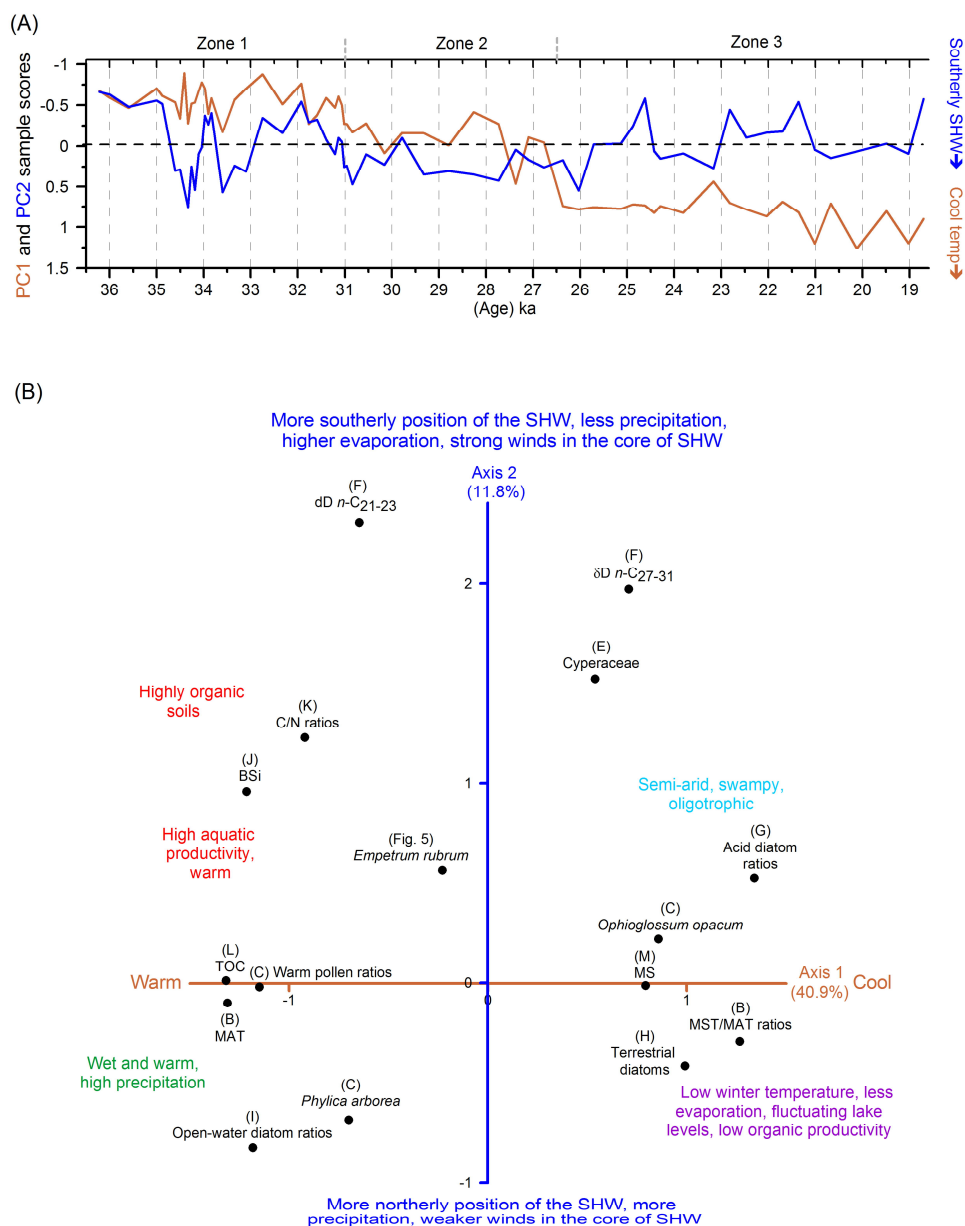
366
367
368 **Figure 5.** Pollen diagram from 1st Pond, Nightingale Island. The diagram shows relative abundance (%)
369 of the pollen taxa. Note that it is both related to depth (cm) and age (ka) on the y-axis, the latter according
370 to the age-depth model in Fig. 3.
371

372 To evaluate changes in the degree of weathered material we used a modified
373 Chemical Index of Alteration (CIA) (Fig. 4D). The long-term development can be divided
374 into three phases with initially low but very variable values until 31 ka, a second phase with
375 stable intermediate CIA values until 27 ka, followed by higher and varying values (Fig. 4D).
376 Magnetic susceptibility (MS) shows centennial-millennial oscillations superimposed on an
377 increasing trend from the bottom to the top of the core (Fig. 4M), and is an indicator of in-
378 washed mineral matter from magnetite-rich basaltic rocks of the catchment. The values of



379 total organic carbon (TOC) and biogenic silica (BSi) (Figs. 4L and J) reflect organic and
380 aquatic productivity in and around the lake with highest values in the oldest section. TOC
381 shows a general decline and BSi oscillates with higher values until 28 ka, after which it
382 gradually drops. The fairly high C/N ratios (Fig. 4K), with a mean value of 17.6, show that
383 organic matter is a mix of terrestrial and aquatic sources. The high and oscillating ratios in the
384 older section followed by a gradual decline implies terrestrial sources dominating until 28 ka,
385 after which time aquatic sources become more important. With respect to stable isotopes (Fig.
386 S1), the high $\delta^{15}\text{N}$ values imply a marine origin possibly related to presence of marine birds,
387 such as Great Shearwater and Albatrosses which have a great impact on the Ponds today,
388 suggesting a more or less continuous impact of SHW. Rising $\delta^{13}\text{C}$ values at 25.7 ka are
389 consistent with the declining C/N ratios after 28 ka, i.e. more aquatic material with enriched
390 ^{13}C , and possibly higher influence from C_4 grasses.

391 Unlike the pollen record (Fig. 5), the diatom record shows large shifts and the 33
392 diatom taxa (Fig. S2) have been classified into three environmental forms. Changes in these
393 groups imply shifts in aquatic and environmental conditions in and around the lake. They
394 show a lake with open water early in the record, followed by shifting lake levels between 35-
395 33 ka (Fig. 4I), supported by δD values of long- and mid-chain *n*-alkanes (Fig. 4F). At 31 ka
396 the open water ratios drop and reach a minimum at 29 ka, in anti-phase with the acid water
397 diatom ratios (Fig. 4G), followed by a rise until 26.6 ka. Thereafter acid species dominate, as
398 oligotrophic wetland encroached around the lake, while periods of more terrestrial diatoms
399 imply episodes of in-washed diatoms from the surroundings. Around 21.2 ka more open water
400 conditions prevail again with high ratios 19-18.6 ka, before the lake dried out (Ljung et al.,
401 2015). The shifts in diatom communities shows that 1P went through substantial hydrologic
402 changes, some of which were rapid, induced by changing P/E ratios, in contrast to the fairly
403 stable vegetation around the lake as seen in the pollen record.



404
 405
 406
 407
 408
 409
 410
 411
 412
 413
 414

Figure 6. Principal component analysis (PCA) of 16 proxies from 1st Pond. (A) Scores of the first two principal components related to age and the three PCA zones. Note that negative values point upwards and how PC1 and PC2 values relate to temperatures and SHW to the right y-axis. (B) PCA plot shows the loadings of the 16 proxies (shown as black dots and black text with reference to proxies in Fig. 4, except for *Empetrum rubrum*). PC1 (red brown) and PC2 (blue) accounts for 40.9 and 11.8% of the variance, respectively. The interpretations of the two axes are shown by red brown and blue texts, and the interpretations of the four segments are based on the combined positions of the proxies in the plot, and are shown in four different colors. MST/MAT=mean summer temperature/mean annual temperature, i.e. a proxy for low winter temperatures.

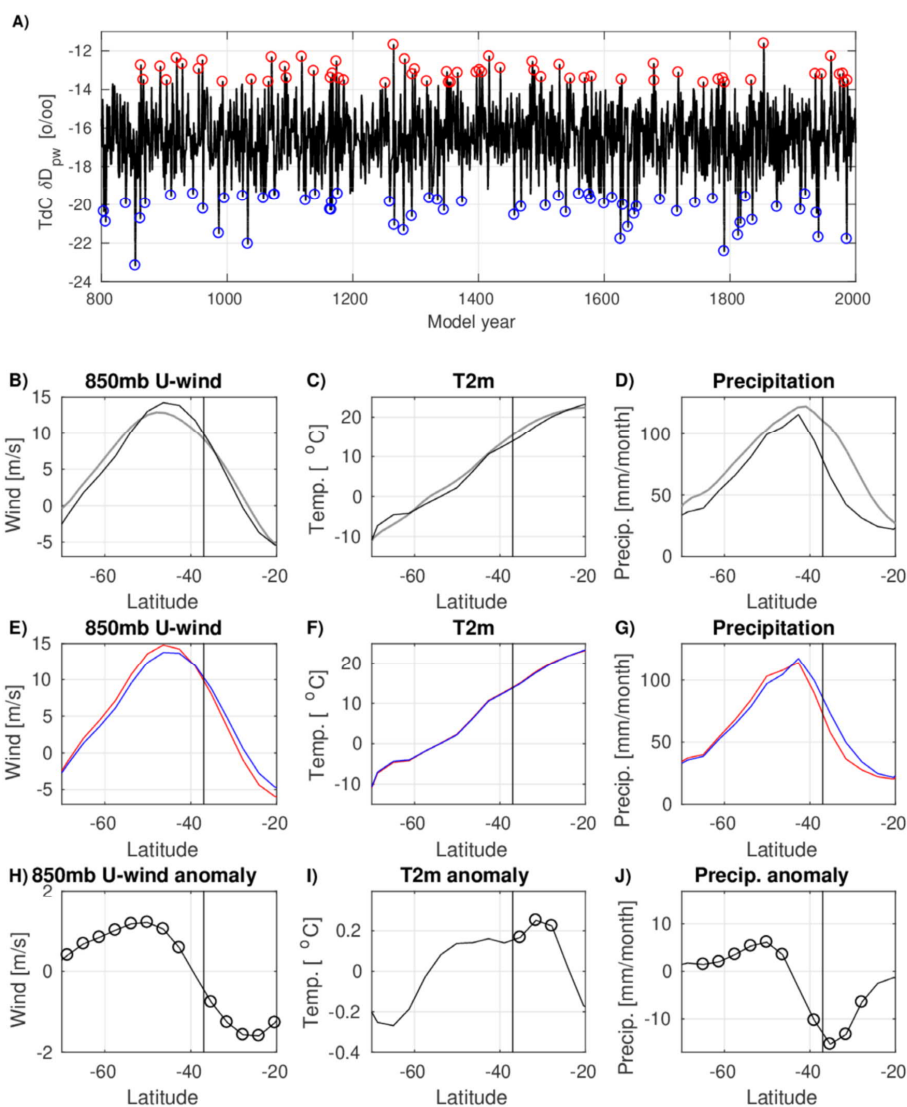


415 **4.2 Linking the Nightingale Island record to South Atlantic hydroclimate**
416 The hydrological sensitivity of a basin like 1P makes it ideal to place local changes into the
417 context of regional hydroclimate shifts. To analyze the variability through time Principal
418 Component Analysis (PCA) was carried out on a data set with 16 hydroclimate-sensitive
419 proxies resulting in 3 PCA zones (Fig. 6A). Note that resolution of the PCA record depends
420 on the proxy with least common sample levels (Table S2), in this case biomarker analyzes.
421 Therefore the temporal resolution of the PCA is not as high as some ice core and marine
422 records. Based on the proxy loadings in the PCA plot (Fig. 6B), it can be divided into four
423 different segments with variable hydroclimate and environmental conditions. The importance
424 of temperature proxies on Axis 1 (40.9% of the variance) is obvious where reconstructed
425 MAT, warm pollen ratios, *Phyllica arborea* pollen, BSi, TOC and open-water diatoms show
426 warm humid conditions to the left (negative) in the biplot (Fig. 6B), vs cooler and drier to the
427 right. The latter is accentuated by *Ophioglossum* spores, a fern growing at high and cold
428 altitudes on TdC, and colder winter temperatures implied by the MST/MAT ratio. Axis 2
429 (11.8% of the variance) is linked to hydrologic indicators being dominated by the δD values
430 of the aquatic $n\text{-C}_{21-23}$ and terrestrial $n\text{-C}_{27-31}$ alkanes (Fig. 6B). We interpret higher δD values
431 (positive axis 2 values) to show stronger influence of more local air masses, with more
432 evaporation and semi-arid conditions, also shown by *Empetrum rubrum* pollen in the upper
433 left quadrant, while the upper right quadrant of the plot shows an acid oligotrophic swampy
434 setting. The segment to the lower right in Figure 6B displays cold conditions and in-wash of
435 terrestrial diatoms as an effect of higher lake level during episodes of more precipitation. The
436 lower left represents warm and wet conditions, implied by *P. arborea* pollen and open water
437 diatoms, and in general, negative axis 2 values relate to more negative δD values.

438

439

440

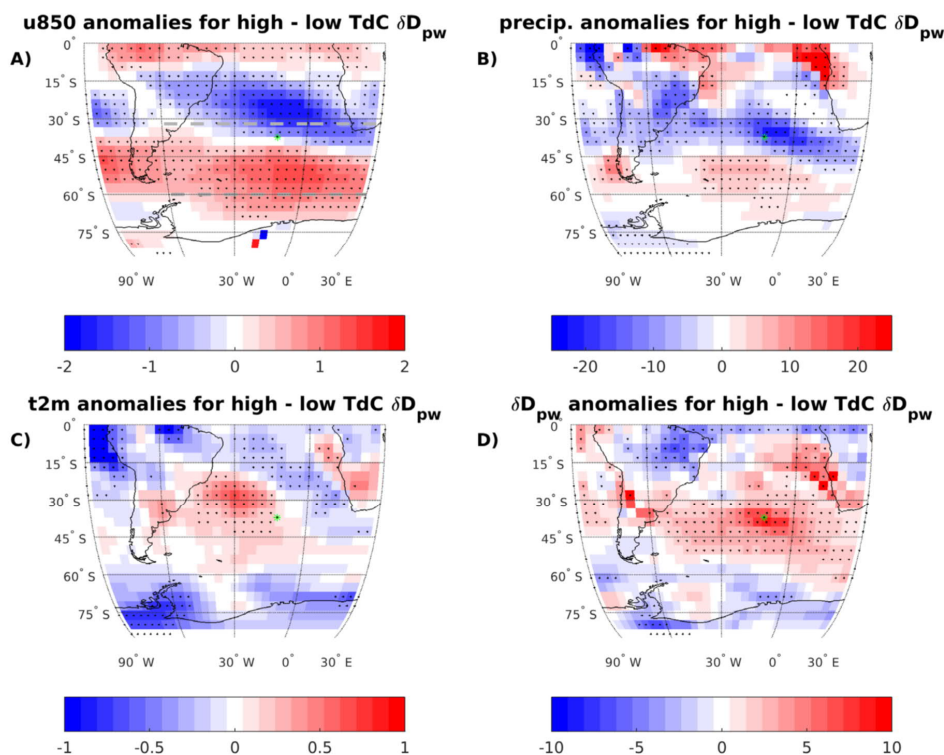


441

442 **Figure 7.** Zonal mean changes in wind, temperature and precipitation related to δD variability at TdC.
 443 A) Time series of simulated precipitation weighted annual mean δD at TdC, with values above and
 444 below the 95th percentile indicated with red and blue circles, respectively. This selection of high and low
 445 δD is used to define the data in figures E-G. (B-D) Annual modeled (black) South Atlantic zonal mean
 446 (30°W to 0°W) westerly wind speed (850mb U-wind, positive towards east), 2m temperature (t2m) and
 447 precipitation compared to the 20th Century Reanalysis climatology 1981-2010 (Compo et al., 2011). (E-
 448 G) Composites of annual modeled zonal mean (30°W to 0°W) westerly wind speed (850mb U-wind),
 449 2m temperature (t2m) and precipitation for high (red) and low (blue) δD at TdC defined in (A). (H-J)
 450 High-minus-low anomalies of model output are shown in (E-F). Circles indicate significant anomalies
 451 ($p < 0.01$) calculated using two-tailed Student's t-test. The vertical bars in (B-J) show the latitude of NI
 452 at 37°S.



453 Observations of the isotopic content of precipitation are very sparse around TdC.
454 Therefore we have investigated the hydroclimate variability with an isotope enabled climate
455 model. To illustrate the relation between the position of the westerlies and the isotopic
456 composition of precipitation at TdC in the simulation, we selected extreme values of high and
457 low δD at TdC (Fig. 7A), and made composite anomalies of the annual mean westerly wind
458 strength at 850mb (u850mb, Fig. 7A), precipitation (Fig. 7B), 2m temperature (t2m, Fig. 7C)
459 and precipitation weighted δD (Fig. 7D) for high-minus-low δD at TdC. This shows that the
460 variability of δD in precipitation at TdC is only weakly dependent on local temperature.
461 Instead, shifts in δD at TdC are related to large scale changes in precipitation and the position
462 of the westerlies. Positive δD anomalies at TdC imply a more southern position of the core of
463 the westerlies with drier conditions at TdC, and negative δD anomalies at TdC denote a more
464 northern position of the core of the westerlies bringing more polar air masses with wetter
465 conditions at TdC. From Figs. 7 and 8, we note that the shifts in TdC precipitation are
466 governed by the precipitation zone on the northern flank of the westerlies shifting with the
467 position of the westerlies themselves. We therefore conclude that our model analysis shows
468 that isotope variability in precipitation at TdC is mainly related to shifts in large scale
469 circulation. High δD values at TdC imply a more southerly SHW position with stronger winds
470 in its core, while low δD values show a more northerly SHW position with weaker winds
471 (Figs. 7E and H). Our analysis also shows that high (low) δD values are related to less (more)
472 precipitation at TdC, but shows little dependency on temperature (Figs. 7F and I, and 8C).
473 The modelled relationship between δD and precipitation corresponds well to the PC2
474 variability of the proxies (Fig. 6B); for example high PC2 and δD values relate to more
475 Cyperaceae (lake overgrowth) and *Empetrum* pollen values (arid soils) and more acid diatoms
476 (swampy), while low PC2 values relate to open-water (lake) and terrestrial (flushed-in)
477 diatoms.



478
479 **Figure 8.** Composite maps of changes in wind, precipitation, temperature and δD related to δD
480 variability at TdC, showing annual anomalies based on composites for high and low δD at TdC (see
481 Figure 7A). A) Westerly wind speed (850mb U-wind, positive towards east, [m/s]). The dashed gray
482 lines show the approximate northern and southern boundaries of the westerlies (850mb U-wind > 5 m/s)
483 to clarify that high TdC δD is related to a southward shift in the westerlies. B) Precipitation [mm/month].
484 C) 2m temperature (t2m, [°C]). D) precipitation weighted δD [%]. Stippling indicates significant
485 anomalies ($p < 0.01$) calculated using a two-tailed Student's t-test. The green spot shows the position of
486 TdC.

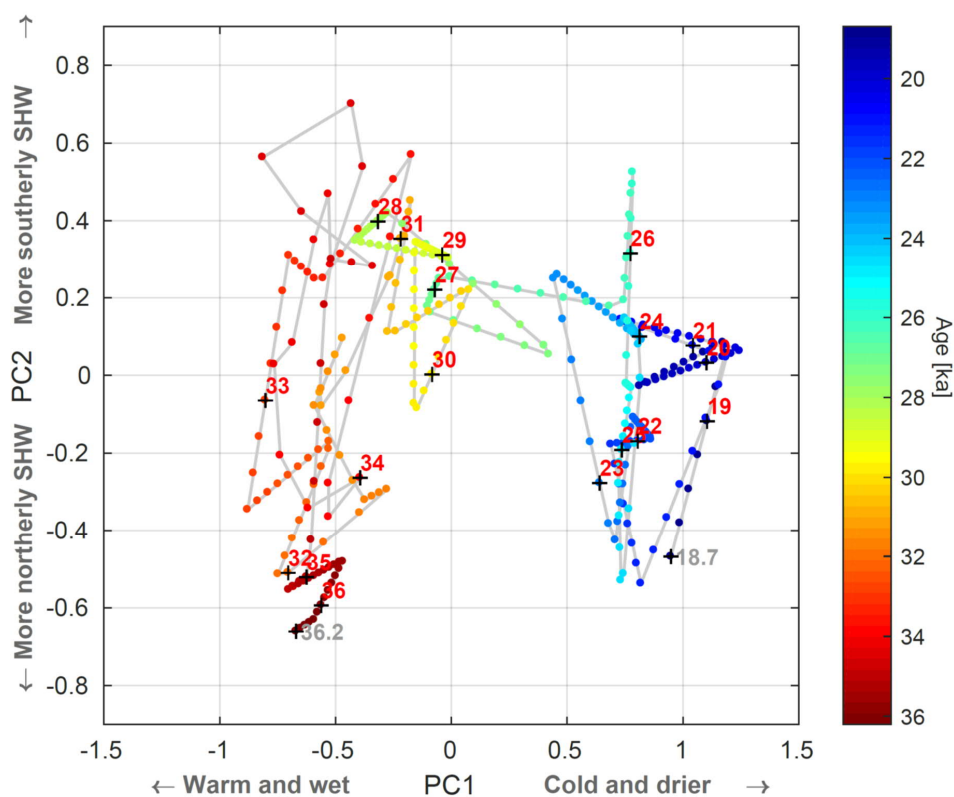
487 5 Hydroclimate correlations and interpretations

488 5.1 The large-scale hydroclimate pattern

489 The three PCA zones displayed in Figures 6A and 9, dated to 36.2-31.0, 31.0-26.5 and 26.5-
490 18.6 ka, show a trend and pattern which is recognizable in much of our data set as well as in
491 the EDML (Fig. 4A) and South Atlantic marine record (Fig. 10B). Zone 1 is fairly warm but
492 oscillates between low and high PC2 values, related to more northerly and weaker SHW, and
493 more local air masses with stronger westerlies in a more southern position, respectively. Zone



494 2 is generally more stable with some minor oscillations with more southerly SHW and
495 corresponds largely to the fairly warm period in Antarctica with the three isotope maxima
496 AIM4.1, AIM4 and AIM3 (Fig. 4A), and a stable and mild period in the South Atlantic marine
497 realm (Fig. 10B). Zone 3 shows a cooling trend, also visible in the EDML and marine record,
498 with variable SHWs. It appears that TdC was continuously influenced by the SHW, as shown
499 by the absence of arid conditions and generally low δD values, verified by humid conditions
500 in southwestern-most Africa throughout most of MIS3 and MIS2 (Chase and Meadows,
501 2007). Apart from the resemblance between the long-term trends in Antarctic ice core data
502 and marine data at 41°S in the South Atlantic (Barker and Diz, 2014) with our data it is, in
503 spite of our lower resolution, interesting to compare our PC2 and $\delta Dn-C_{C27-C31}$ records (Figs.
504 4A and 10G) with other regional records related to SHWs. Taking age uncertainties of a few
505 hundred years into account we note a resemblance with marine Fe fluxes at 42°S (Martínez-
506 García et al., 2014) where low δD values (Fig. 10G) co-vary with high Fe fluxes (Fig. 10F)
507 due to northerly SHW in a cooler Southern Hemisphere, thus expanding the Patagonian dust
508 source. Similar co-variability can be seen in the $\delta^{18}O$ record on fluid inclusions of SE
509 Brazilian speleothems (Millo et al., 2017) where low values (Fig. 10E) imply strengthening of
510 the monsoon shifting the South Atlantic atmospheric system southwards, including SHW. We
511 also note that the Antarctic CO₂ record (Fig. 10C) and the [CO₃²⁻] record (Gottschalk et al.,
512 2015) from the South Atlantic (Fig. 10D), inferring AMOC strength and Southern Ocean
513 ventilation, share similarities with our SHW records, as described in the section below.
514



515
516
517
518
519
520
521
522

Figure 9. Parametric plot of the PC1 and PC2 sample values as a function of time shown by the color bar to the right. Red numbers denote each ka with grey numbers at the start and end of the plot. Data was interpolated to 50-year time steps to illustrate rate of change; the larger distance between dots the more rapid change. Note that the hydroclimate interpretations from Figure 6B are shown on the two PC axes.

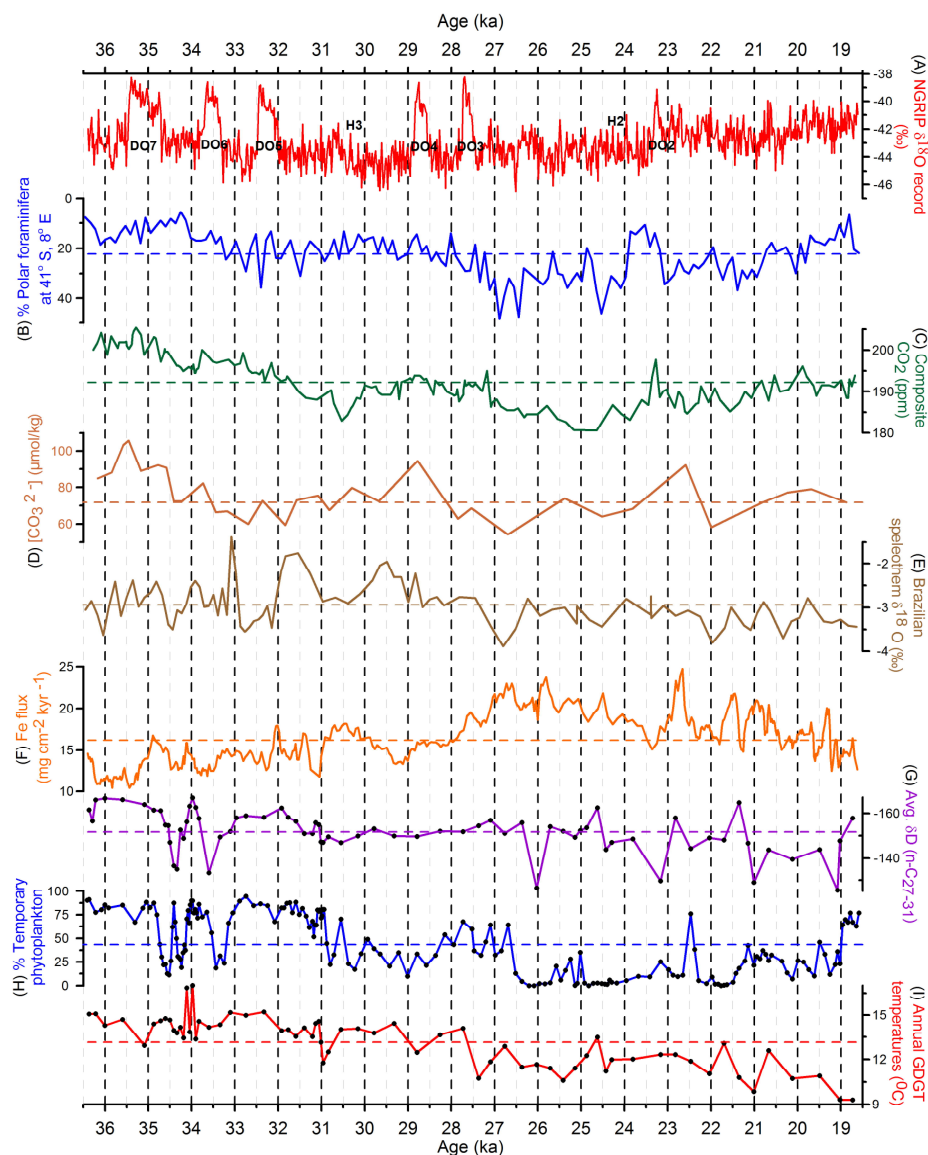
523 5.2 A detailed hydroclimate scenario for the central South Atlantic

524 Due to chronological uncertainties in all records, lower resolution in some records and the
525 complex phase-relationships during abrupt interhemispheric climate shifts (Markle et al.,
526 2016), detailed comparison of short-term variations across sites has to be treated with caution.
527 In spite of these short-comings we will present a scenario based on our record and likely
528 correlations.

529 The start of our record shows warm and wet conditions with northerly SHW,
530 coinciding with the long and warm AIM7 followed by a cooling (Fig. 10J) at the onset of



531 DO7. This is followed by the very dynamic period 35-33 ka, shown by high sedimentation
532 rates (Fig. 3) and peak variability in terms of both rapidity and amplitude (Fig. 9). Such
533 variability is also seen in marine and ice core records, and in spite of the age uncertainties at
534 34-35 ka (Fig. 3) we tentatively correlate this period in our record to the end of DO7 and the
535 minimum between AIM6 and AIM7. This corroborates the overlaps and time lags that have
536 been postulated for DO and AIM events (Markle et al., 2016; Pedro et al., 2018; WAIS
537 Divide Project Members, 2015). At 34 ka we note a temperature peak at the onset of AIM6
538 (Figs. 4 and 11) followed by falling temperatures, δD , Fe flux and CO_2 values and high
539 humidity (Figs. 10G, F, C and H). This change reflects northerly and weaker westerlies, with
540 rising speleothem $\delta^{18}O$ and WAIS d_{in} values (Figs. 10E and 11E), denoting the start of DO6
541 with a warming of the NH (Fig. 10A). This caused northwards shifting ITCZ and SHW in line
542 with the theory that the atmospheric circulation system moves towards the warmer
543 hemisphere, responding to the change in the cross-equatorial temperature gradient (McGee et
544 al., 2014). At 33.5 ka we see a southward SHW shift with rising temperatures and higher CO_2
545 and lower WAIS d_{in} values with dry conditions. We relate this to the onset of AIM5; a
546 warming which is interrupted at 32.8 ka by a northerly SHW shift and wetter conditions (Figs.
547 11F and 10H) possibly triggered by DO5. This partly continues until 31.7 ka when SHW
548 moves south with a minor temperature rise (Fig. 11D) and decreasing humidity, possibly as a
549 response to the post-DO5 cooling (Fig. 10A). The high variability and large amplitude of the
550 changes of Zone 1 (Fig. 9) have facilitated conceivable correlations to other records. Based on
551 these we can conclude that at large, PC2 implies northerly shift of the SHW during warm
552 North Atlantic periods, and a more southerly position during warm periods in Antarctica, also
553 in line with interpretation of Antarctic deuterium excess data (Markle et al., 2016).



554
 555 **Figure 10.** Comparisons between other proxy records (A-F) and Nightingale Island proxies for SHW
 556 (G), wetness (H) and temperature (I), with mean values as broken lines. (A) $\delta^{18}\text{O}$ values from the NGRIP
 557 ice core (Andersen et al., 2006) showing DO and H events. Ice core records are on a common time scale
 558 (Veres et al., 2013). (B) Abundance (%) of polar foraminifera at 41°S in the S Atlantic (Barker and Diz,
 559 2014). (C) Composite Antarctic CO_2 record from Siple Dome (Ahn and Brook, 2014) and WAIS (Stenni
 560 et al., 2010). (D) $[\text{CO}_3^{2-}]$ data at 44°S in the South Atlantic (Gottschalk et al., 2015). (E) Speleothem ^{18}O
 561 record on fluid inclusions from SE Brazil (Millo et al., 2017). (F) Fe flux data in the South Atlantic at
 562 42°S (Martínez-García et al., 2014). Then follow NI data, (G) Average δD values for the terrestrial n -
 563 C_{27-31} alkanes. (H) Abundance (%) of temporary phytoplanktonic diatoms implying relative water depth.
 564 (I) Annual NI temperatures from the GDGT analyses. Note that that sample levels are shown by a dot
 565 in (G)-(I) and that y-axes of (B) and (G) show higher values downwards to facilitate comparisons to
 566 other proxies.



567 The Zone 1/Zone 2 boundary at 31 ka (Fig. 6A) is a dynamic transition, shown
568 by many proxies and peak sedimentation rates (Figs. 9 and 3). The 4.5 ka long and stable
569 Zone 2 (Fig. 6A) is characterized by fairly high but slightly decreasing temperatures and as in
570 Zone 1 a dominating southerly SHW position. It is possible, taking age uncertainties into
571 account, that H3 at 30.5 ka (Fig. 10A) triggered the southbound SHW and the rising CO₂ and
572 MAT values, and the reduced humidity between 31-30 ka (Figs. 11F, 10C, 10I and 10H). The
573 following long and warm AIM4 may have stabilized conditions in the South Atlantic in spite
574 of the DO4 event at 28.8 ka. This stability is also seen in marine records (Fig. 10B), and the
575 rather stable southern position of the SHW agrees with the fairly high CO₂ values between 30-
576 27.2 ka and with falling and rather low Fe fluxes (Fig. 10F). We also note higher lake
577 evaporation from δD values of the aquatic *n*-C₂₃ (Fig. 4F), in concert with rising summer
578 insolation (Fig. 11A). Around 27.5 ka we see a brief response in some of the proxies to the
579 short DO3 event (Fig. 10A), such as the MAT and PC2 records (Figs. 11D and F) and is also
580 noticeable in e.g. the marine and Brazilian monsoon records (Figs. 10B and E).

581 The start of Zone 3 constitutes the most drastic change in our record (Figs. 6A
582 and 9) but timing varies between proxies (Fig. 4). MAT, TOC and C/N ratios start to decrease
583 already at 28 -27.5 ka, coinciding with DO3, the biologic proxies (Figs. 4C and G-J, Fig. S2)
584 respond slightly later possibly because they do not react until certain hydroclimate thresholds
585 for the vegetation and algae flora are reached. The Zone 2-3 transition is roughly
586 simultaneous with the onset of LGM in Antarctica (Fig. 10C), when 1P switched from a lake
587 to a wetland, coinciding with increased abundance of polar foraminifera at 41°S (Fig. 10B).
588 This may be an effect of the STF moving north of TdC, a meridional shift comparable to what
589 has been shown from the eastern Pacific (Kaiser et al., 2005). The fairly stable PC1 values
590 show cool and less humid LGM conditions, while the variable PC2 values imply shifts in the
591 position of SHW (Fig. 11F). There is also a good correspondence between our δD (*n*-C₂₇₋₃₁)



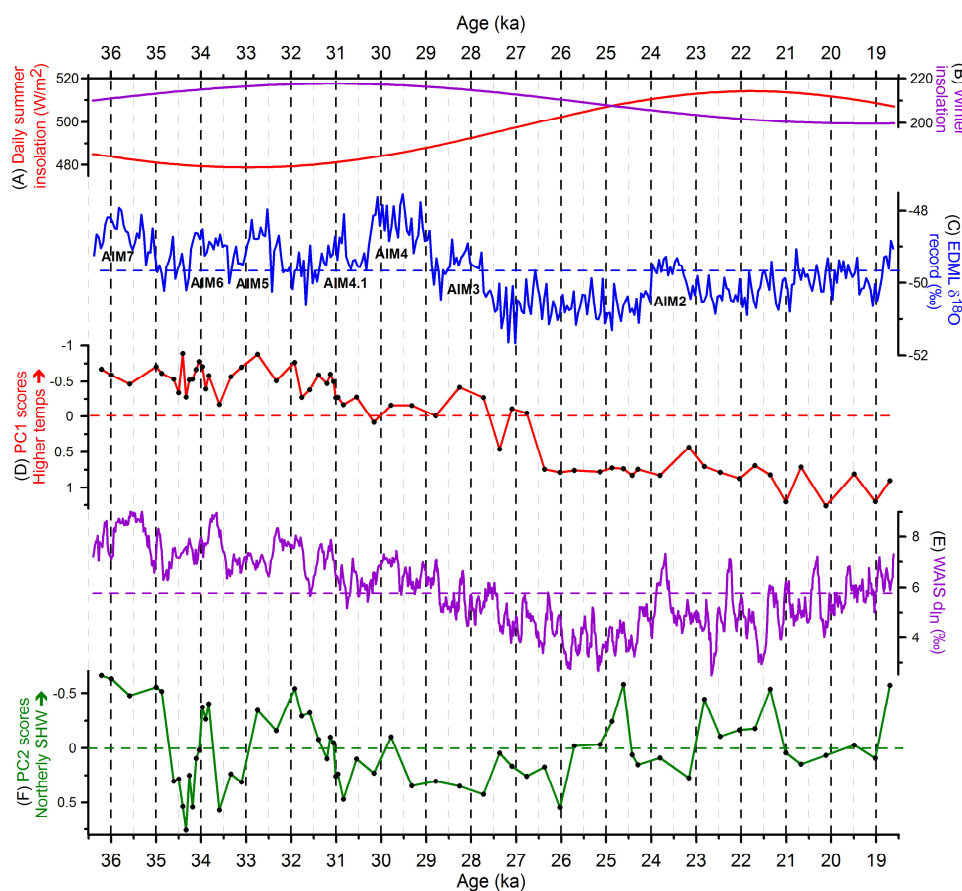
592 maxima after 27 ka and Fe flux minima from the South Atlantic (Figs. 10G-F), both indicating
593 southerly shifts of SHW. During this period our data also show generally higher mean δD (n-
594 C_{27-31}) values than in Zone 1, implying a more southern position of SHW during the Antarctic
595 LGM, as seen in some modeling results (e.g. Sime et al., 2016). This is also compatible with
596 the fact that the LGM temperature lowering in the Northern Hemisphere (Johnsen et al., 1995)
597 was much larger than in the south (Stenni et al., 2010), shifting the atmospheric system to the
598 south due to changes in the cross-equatorial gradient (McGee et al., 2014), as implied by the
599 speleothem $\delta^{18}O$ data (Fig. 10E) showing increased precipitation (Millo et al., 2017).

600 After 26.5 ka we note phases of less humid swampy oligotrophic conditions on
601 NI at 26, 24.5-23, 22 and 20.5-19 ka (Fig. 10H) interrupted by periods of more or less open
602 water, possibly driven by shifts of SHW. The former often show enriched δD values (Fig.
603 10G), while the latter were characterized by higher precipitation and more depleted δD
604 values. Regarding the response of CO_2 to these SHW shifts we note a fairly good agreement
605 between low/falling CO_2 values and a northerly SHW position, and vice versa. For example,
606 the CO_2 minimum at 24.5-25 ka (Fig. 10C) matches with an extreme northern SHW position
607 (Figs. 10G and 11F), and the CO_2 peak at 23.3 ka agrees with the end of a long phase of
608 southwards moving SHW. The latter might have been triggered by the onset of H2 at 24.1 ka
609 (Fig. 10A) followed by the inception of AIM2 (Fig. 11C).

610 The absence of *P. arborea* (Figs. 4C and 5) and our temperature proxies (Fig.
611 4B) imply that minimum winter temperatures at our site were occasionally below zero,
612 especially after 26 ka; periods of frost also explain increased weathering (Fig. 4D). Between
613 23 and 19 ka the Antarctic winter sea ice reached 47°S in the South Atlantic (Gersonde et al.,
614 2005), only some 1000 km south of TdC. Our 1P record shows a declining temperature trend
615 during the end of this period (Fig. 10I), in contrast to rising temperatures in Antarctica and
616 South Atlantic (Figs. 11C and 10B). This regional temperature anomaly may be explained by



617 the declining summer insolation at the latitude of Tristan da Cunha (Fig. 11A), and may also,
618 at the end of LGM, be related to break-up of Antarctic ice shelves as sea levels rose, causing
619 cooler conditions further north. In fact, temperature minima after 19 ka are seen in both our
620 record and in marine data (Figs. 10I and B), as well as a δD minimum (Fig. 10G).



621 **Figure 11.** Comparison between our PC1 and PC2 records and other relevant data. (A and B) Mean daily
622 summer and winter insolation at 37°S (Laskar et al., 2004). (C) EDML $\delta^{18}\text{O}$ record (EPICA Community
623 Members et al., 2006) with Antarctic Isotope Maxima (AIM). (D) PC1 scores implying temperature
624 shifts at NI. (E) WAIS d_{in} values from west Antarctica (Markle et al., 2016). (F) PC2 scores indicate
625 impact of SHW at NI. Note that sample levels, i.e. time resolution, for the PC records are shown as dots.
626
627

628

629



630 **5.3 A climate synthesis**

631 In general, our data implies two main climate modes for the study period, separated by a
632 transition period 31-26.5 ka, Zone 2. This is displayed in Figure 9, with pre-LGM (Zone 1)
633 clearly separated from the LGM period (Zone 3) on Axis 1, but also with higher variability of
634 the pre-LGM period. This variability is possibly related to an active bipolar seesaw
635 mechanism during Zone1/MIS3 even at the fairly low latitudes of TdC, triggering N-S shifts
636 of SHW and related hydroclimate conditions. Any CO₂ effects from the rapid SHW shifts in
637 Zone 1 are not discernible, but the dominating more northern SHW position may have
638 resulted in the general CO₂ decline (Fig. 10C). With the onset of Zone 2 there may be a
639 stronger link between CO₂ and SHWs. In view of carbon-cycle time lags, the mainly
640 southerly positioned and more intense SHW at 31-27.5 ka (Fig. 11F) may have resulted in the
641 rising and higher CO₂ concentrations at 30.5-27.2 ka (Fig. 10C), with more upwelling, CO₂
642 outgassing and less sea ice. The LGM mode is characterized by falling and low temperatures,
643 lack of clear effects of the bipolar seesaw mechanism, possibly due to the much stronger
644 cooling in the north as the cross-equatorial gradient changed. The variability is mainly related
645 to proxies associated with SHW changes, as summarized by PC2, with a similarly high
646 frequency variability of WAIS d_{in} and Fe fluxes (Figs. 11E, 10F), with resulting CO₂
647 variability. However, a key difference between our SHW proxies (PC2) and the WAIS d_{in}
648 record is that the latter represents SHW variability superimposed on large scale temperature
649 trends while our PC2 record reflects the SHW signal without temperature impact.

650 Thus, the largest change in our record occurs after 27.5 ka when the effects of
651 the strong post-DO3 cooling of the Northern Hemisphere start dominating the hydroclimate of
652 the South Atlantic with highly variable SHW after 25 ka ; possibly a prerequisite for the
653 oscillating CO₂ levels after the CO₂ minimum at 25 ka (Fig. 10C).



654 **6. Conclusions**

655 Our 1P data, reflecting terrestrial and aquatic responses to shifting atmospheric conditions,
656 show that the glacial hydroclimate of South Atlantic mid-latitudes experienced varying
657 degrees of humidity, but with more or less continuous impact of SHW. Temperature
658 conditions were in general warm but oscillating during MIS3, with shifting strength and
659 positions of the westerlies. Weaker and northwards moving SHW at the onset of NH
660 interstadials with stronger and southerly westerlies during NH stadials partly reflect the
661 complex processes behind phase relationships between Greenland and Antarctic ice core
662 climate records (Pedro et al., 2018). These shifts, possibly triggered by changes in the cross-
663 equatorial gradient, are to some extent manifested by rising (falling) CO₂ levels when SHW
664 was stronger (weaker) and located more towards the south (north), in line with Holocene
665 records (Saunders et al., 2018). The largest variability in our record is seen during the fairly
666 warm and humid period 36.5-31 ka with frequent and abrupt shifts, followed by a fairly stable
667 period 31-27 ka with slowly declining temperatures and dominating southerly SHWs. The
668 largest over-all change occurs after 27 ka, exhibited by a distinct cooling trend. This early
669 mid-latitude cooling is in phase with LGM in Antarctica, consistent with some modeling
670 results (Fogwill et al., 2015). We think this represents a mode shift in hydroclimate; from the
671 highly variable MIS3 conditions through the more steady conditions 31-27 ka (Figs. 11D and
672 F) into LGM with its cool and less humid climate, perhaps as a result of the SF moving north
673 of TdC. The variable position of SHW (Fig. 11F), with particularly high δD values at 26, 23.1,
674 21 and 19.1 ka (Fig. 10G), is noteworthy, inferring fairly sudden and distinct southerly shifts
675 of the westerlies. The end of our record shows that cool conditions persisted in these SH mid-
676 latitudes until at least 18.6 ka. This might have been a combined effect of declining summer
677 insolation and northward shifting westerlies (Figs. 11A and F), conveying cold air masses, sea
678 ice and ice bergs far north from collapsing Antarctic ice shelves (Weber et al., 2014).

679



680 **Author contributions.** S.B. was the initiator of the study, received funds, drilled and described cores,
681 carried out sampling and XRF analyses and contributed with most writing, J.S. contributed with
682 interpreting data, much writing, ran the isotope model experiment (ECHAM5-wiso/MPI-OM) and
683 analyzed all modeling results, K.L. drilled and described cores, carried out sampling, analyzed C, N,
684 ¹³C, ¹⁵N, pollen and contributed with writing, F.A. contributed with the age model and some writing,
685 R.F. contributed with interpreting and analyzing diatom results and some writing, R.H.S. helped
686 interpret biomarkers and hydrogen isotopes and contributed with some writing, M.E.K. analyzed XRF
687 results and contributed with some writing, T.F.S. contributed with creative inputs and some writing,
688 S.H. sampled and carried out diatom analyzes, H.J. carried out multivariate statistics, Y.K.K.A.
689 analyzed biomarkers and hydrogen isotopes, R.M. calculated insolation values and contributed with
690 little writing, J.E.R. carried out biomarker analyses and calibrated the GDGTs and N.V.d.P. carried out
691 biogenic silica analysis. All commented on the manuscript.

692 **Acknowledgements.** The co- members of the 2010 Tristan expedition (M. Björck, A. Björk, A.
693 Cronholm, J. Haile, M. Grignon) and Tristan islanders are gratefully acknowledged for hard work at
694 sea and on Nightingale I. The isotope enabled climate model, ECHAM5-wiso/MPI-OM, was run at the
695 AWI Computer and Data Center. We thank M. Werner for helping to set up and run the model
696 simulations, S. Barker, F. Cruz and C. Millo for providing us with their data, G. Ahlberg for pollen
697 sample preparations and Å. Wallin for magnetic susceptibility measurements. We are grateful for
698 financial support, incl. expedition costs, from the Swedish Research Council (VR), the Crafoord
699 Foundation, the Royal Fysiographic Society, the LUCCI Centre in Lund and the Lund and Stockholm
700 universities. We dedicate this paper to Charles T. Porter, our skipper on his ketch Ocean Tramp, who
701 challenged all kind of weather in the South Atlantic to retrieve our unique sediment cores. However,
702 he sadly died suddenly in March 2014 while preparing for our next expedition: a great loss in many
703 respects but mostly as an invaluable, memorable friend and colleague.

704

705

706

707

708

709

710

711



712 **References**

713

714 Ahn, J. and Brook, E. J.: Siple Dome ice reveals two modes of millennial CO₂ change during the last
715 ice age, *Nat. Commun.*, 5, 3723, 2014.

716 Andersen, K. K., Svensson, A., Johnsen, S., Rasmussen, S. O., Bigler, M., Röthlisberger, R., Ruth, U.,
717 Siggaard-Andersen, M. L., Steffensen, J. P., Dahl-Jensen, D., Vinther, B. M. and Clausen, H. B.: The
718 Greenland Ice Core Chronology 2005, 15-42 ka. Part 1: Constructing the time scale, *Quaternary Sci.*
719 *Rev.* 25, 3246–3257, doi:<https://doi.org/10.1016/j.quascirev.2006.08.002>, 2006.

720 Anker Björk, A., Björck, S., Cronholm, A., Haile, J., Ljung, K. and Porter, C.: Possible Late
721 Pleistocene volcanic activity on Nightingale Island, South Atlantic ocean, based on geoelectrical
722 resistivity measurements, sediment corings and ¹⁴C dating, *GFF*, 133, 10.1080/11035897.2011.618275,
723 2011.

724 Bard, E. and Rickaby, R. E. M.: Migration of the subtropical front as a modulator of glacial climate,
725 *Nature*, 460, 380–383, doi:[10.1038/nature08189](https://doi.org/10.1038/nature08189), 2009.

726 Barker, S. and Diz, P.: Timing of the descent into the last Ice Age determined by the bipolar seesaw,
727 *Paleoceanography*, 29, 489–507, doi:[10.1002/2014PA002623](https://doi.org/10.1002/2014PA002623), 2014.

728 Battarbee, R. W. and Keen, M. J.: The use of electronically counted microspheres in absolute diatom
729 analysis, *Limnol. Oceanogr.*, 27, 184–188, 1982.

730 Battarbee, R. W., Jones, V. J., Flower, R. J., Cameron, N. G., Bennion, H., Carvalho, L. and Juggins,
731 S.: in *Diatoms*, 155–202, Kluwer Academic Publishers, Dordrecht., 2001.

732 Berglund, B. E. and Ralska-Jasiewiczowa, M.: Pollen analysis and pollen diagrams, in *Handbook of*
733 *palaeoecology and palaeohydrology*, edited by B. E. Berglund, 455–484, John Wiley and sons,
734 Chichester., 1986.

735 Broecker, W. S.: Paleocan circulation during the Last Deglaciation: A bipolar seesaw?,
736 *Paleoceanography*, 13, 119-121, doi:[10.1029/97PA03707](https://doi.org/10.1029/97PA03707), 1998.

737 Bronk Ramsey, C.: Radiocarbon Calibration and Analysis of Stratigraphy: The OxCal Program,
738 *Radiocarbon*, 37, 425–430, doi:[10.1017/S0033822200030903](https://doi.org/10.1017/S0033822200030903), 1995.

739 Bronk Ramsey, C.: Bayesian Analysis of Radiocarbon Dates, *Radiocarbon*, 51, 337–360,
740 doi:[10.1017/S0033822200033865](https://doi.org/10.1017/S0033822200033865), 2009a.

741 Bronk Ramsey, C.: Dealing with Outliers and Offsets in Radiocarbon Dating, *Radiocarbon*, 51, 1023–
742 1045, doi:[10.1017/S0033822200034093](https://doi.org/10.1017/S0033822200034093), 2009b.

743 Ceppi, P., Hwang, Y.-T., Liu, X., Frierson, D. M. W. and Hartmann, D. L.: The relationship between
744 the ITCZ and the Southern Hemispheric eddy-driven jet, *J. Geophys. Res. Atmos.*, 118, 5136–5146,
745 doi:[10.1002/jgrd.50461](https://doi.org/10.1002/jgrd.50461), 2013.

746 Chase, B. M. and Meadows, M. E.: Late Quaternary dynamics of southern Africa's winter rainfall
747 zone, *Earth Sci. Rev.*, 84, 103–138, doi:[10.1016/j.earscirev.2007.06.002](https://doi.org/10.1016/j.earscirev.2007.06.002), 2007.

748 Chiang, J. C. H., Lee, S.-Y., Putnam, A. E. and Wang, X.: South Pacific Split Jet, ITCZ shifts, and
749 atmospheric North–South linkages during abrupt climate changes of the last glacial period, *Earth*
750 *Planet. Sci. Let.*, 406, 233–246, doi:[10.1016/j.epsl.2014.09.012](https://doi.org/10.1016/j.epsl.2014.09.012), 2014.



- 751 Compo, G. P., Whitaker, J. S., Sardeshmukh, P. D., Matsui, N., Allan, R. J., Yin, X., Gleason, B. E.,
752 Vose, R. S., Rutledge, G., Bessemoulin, P., Brönnimann, S., Brunet, M., Crouthamel, R. I., Grant, A.
753 N., Groisman, P. Y., Jones, P. D., Kruk, M. C., Kruger, A. C., Marshall, G. J., Mauger, M., Mok, H. Y.,
754 Nordli, Ø., Ross, T. F., Trigo, R. M., Wang, X. L., Woodruff, S. D. and Worley, S. J.: The Twentieth
755 Century Reanalysis Project, *Q. J. Roy. Meteor. Soc.*, 137, 1–28, doi:10.1002/qj.776, 2011.
- 756 Conley, D. and Schelske, C. L.: Biogenic silica, in *Tracking environmental change using lake*
757 *sediments; volume 3, terrestrial, algal, and siliceous indicators*, vol. 3, Kluwer Academic Publishers,
758 Dordrecht., 2001.
- 759 De Jonge, C., Hopmans, E. C., Zell, C. I., Kim, J.-H., Schouten, S. and Sinninghe Damsté, J. S.:
760 Occurrence and abundance of 6-methyl branched glycerol dialkyl glycerol tetraethers in soils:
761 Implications for palaeoclimate reconstruction, *Geochim. Cosmochim. Ac.*, 141, 97–112,
762 doi:10.1016/j.gca.2014.06.013, 2014.
- 763 Ebisuzaki, W.: A method to estimate the statistical significance of a correlation when the data are
764 serially correlated, *J. Climate*, 10, 2147–2153, doi:10.1175/1520-
765 0442(1997)010<2147:AMTETS>2.0.CO;2, 1997.
- 766 EPICA Community Members: One-to-one coupling of glacial climate variability in Greenland and
767 Antarctica, *Nature*, 444, 195–198, doi:10.1038/nature05301 <<http://doi.org/10.1038/nature05301>> ,
768 hdl:10013/epic.41684, 2006.
- 769 Fogwill, C. J., Phipps, S. J., Turney, C. S. M. and Golledge, N. R.: Sensitivity of the Southern Ocean
770 to enhanced regional Antarctic ice sheet meltwater input, *Earth. Future*, 3, 317–329,
771 doi:10.1002/2015EF000306, 2015.
- 772 Gersonde, R., Crosta, X., Abelmann, A. and Armand, L.: Sea-surface temperature and sea ice
773 distribution of the Southern Ocean at the EPILOG Last Glacial Maximum—a circum-Antarctic view
774 based on siliceous microfossil records, *Quaternary Sci. Rev.*, 24, 869–896,
775 doi:10.1016/j.quascirev.2004.07.015, 2005.
- 776 Gottschalk, J., Skinner, L. C., Misra, S., Waelbroeck, C., Meniel, L. and Timmermann, A.: Abrupt
777 changes in the southern extent of North Atlantic Deep Water during Dansgaard–Oeschger events, *Nat.*
778 *Geosci.*, 8, 950–954, doi:10.1038/ngeo2558, 2015.
- 779 Grasshoff, K., Erhardt, M. and Kremling, K.: *Methods of sea water analysis*, Verlag Chemie., 1983.
- 780 Hafsten, U.: *Pleistocene development of vegetation and climate in Tristan de Cunha and Gough Island*,
781 Bergen, 1960.
- 782 Helfert, M., Mecking, O., Lang, F. and von Kaenel, H.-M.: Neue Perspektiven für die
783 Keramikanalytik. Zur Evaluation der portablen energiedispersiven Röntgenfluoreszenzanalyse (P-ED-
784 RFA) als neues Verfahren für die geochemische Analyse von Keramik in der Archäologie., *Frankfurter*
785 *elektronische Rundschau zur Altertumskunde*, (14), 1–30, 2011.
- 786 Hogg, A. G., Hua, Q., Blackwell, P. G., Niu, M., Buck, C. E., Guilderson, T. P., Heaton, T. J., Palmer,
787 J. G., Reimer, P. J., Reimer, R. W., Turney, C. S. M. and Zimmerman, S. R. H.: SHCal13 Southern
788 Hemisphere Calibration, 0–50,000 Years cal BP, *Radiocarbon*, 55, 1889–1903, 2013.
- 789 Johnsen, S. J., Dahl-Jensen, D., Dansgaard, W. and Gundestrup, N.: Greenland palaeotemperatures
790 derived from GRIP bore hole temperature and ice core isotope profiles, *Tellus B: Chem. Phys.*
791 *Meteor.*, 47, 624–629, doi:10.3402/tellus.v47i5.16077, 1995.
- 792 Juggins, S.: *User guide. Software for ecological and palaeoecological data analysis and visualisation*,
793 Newcastle University, Newcastle upon Tyne, UK., 2007.



- 794 Kaiser, J., Lamy, F. and Hebbeln, D.: A 70-kyr sea surface temperature record off southern Chile
795 (Ocean Drilling Program Site 1233), *Paleoceanography*, 20, doi:10.1029/2005PA001146, 2005.
- 796 Krammer, K. and Lange-Bertalot, H.: Süßwasserflora von Mitteleuropa Bacillariophyceae Teil 1-4,
797 Gustav Fischer, Stuttgart., 1986.
- 798 Lambeck, K., Rouby, H., Purcell, A., Sun, Y. and Sambridge, M.: Sea level and global ice volumes
799 from the Last Glacial Maximum to the Holocene, *PNAS*, 111, 15296–15303,
800 doi:10.1073/pnas.1411762111, 2014.
- 801 Lamy, F., Kilian, R., Arz, H. W., Francois, J.-P., Kaiser, J., Prange, M. and Steinke, T.: Holocene
802 changes in the position and intensity of the southern westerly wind belt, *Nat. Geosci.*, 3,
803 doi:10.1038/ngeo959, 2010.
- 804 Lamy, F., Gersonde, R., Winckler, G., Esper, O., Jaeschke, A., Kuhn, G., Ullermann, J., Martinez-
805 García, A., Lambert, F. and Kilian, R.: Increased Dust Deposition in the Pacific Southern Ocean
806 During Glacial Periods, *Science*, 343, 403–407, doi:10.1126/science.1245424, 2014.
- 807 Lange-Bertalot, H.: Diatomeen der Anden / Diatoms of the Andes., 1995.
- 808 Laskar, J., Robutel, P., Joutel, F., Gastineau, M., Correia, A. C. M. and Levrard, B.: A long-term
809 numerical solution for the insolation quantities of the Earth, *Ast. Astrophys.*, 428, 261–285,
810 doi:10.1051/0004-6361:20041335, 2004.
- 811 Le Cohu, R. and Maillard, R.: Les diatomées monoraphidées des îles Kerguelen, *Annal. Limnol.*, 19,
812 143–167, 1983.
- 813 Ljung, K. and Björck, S.: Holocene climate and vegetation dynamics on Nightingale Island, South
814 Atlantic--an apparent interglacial bipolar seesaw in action, *Quaternary Sci. Rev.*, 26, 3150–3166,
815 doi:10.1016/j.quascirev.2007.08.003, 2007.
- 816 Ljung, K., Holmgren, S., Kylander, M., Sjolte, J., Van der Putten, N., Kageyama, M., Porter, C. T. and
817 Björck, S.: The last termination in the central South Atlantic, *Quaternary Sci. Rev.*, 123, 193–214,
818 doi:10.1016/j.quascirev.2015.07.003, 2015.
- 819 Loomis, S. E., Russell, J. M., Ladd, B., Street-Perrott, F. A. and Sinninghe Damsté, J. S.: Calibration
820 and application of the branched GDGT temperature proxy on East African lake sediments, *Earth
821 Planet. Sc. Lett.*, 357–358, 277–288, doi:10.1016/j.epsl.2012.09.031, 2012.
- 822 Markle, B. R., Bitz, C. M., Buizert, C., Steig, E. J., White, J. W. C., Pedro, J. B., Ding, Q.,
823 Schoenemann, S. W., Fudge, T. J., Sowers, T. and Jones, T. R.: Global atmospheric teleconnections
824 during Dansgaard–Oeschger events, *Nat. Geosci.*, 10, 36–40, doi:10.1038/ngeo2848, 2016.
- 825 Martin, J. H. and Fitzwater, S. E.: Iron deficiency limits phytoplankton growth in the north-east Pacific
826 subarctic, *Nature*, 331, 341–343, doi:10.1038/331341a0, 1988.
- 827 Martínez-García, A., Sigman, D. M., Ren, H., Anderson, R. F., Straub, M., Hodell, D. A., Jaccard, S.
828 L., Eglinton, T. I. and Haug, G. H.: Iron Fertilization of the Subantarctic Ocean During the Last Ice
829 Age, *Science*, 343, 1347–1350, doi:10.1126/science.1246848, 2014.
- 830 McGee, D., Donohoe, A., Marshall, J. and Ferreira, D.: Changes in ITCZ location and cross-equatorial
831 heat transport at the Last Glacial Maximum, Heinrich Stadial 1, and the mid-Holocene, *Earth Planet.
832 Sci. Lett.*, 390, 69–79, doi:10.1016/j.epsl.2013.12.043, 2014.
- 833 Millo, C., Strikis, N. M., Vonhof, H. B., Deininger, M., Cruz, F. W. da, Wang, X., Cheng, H. and
834 Edwards, R. L.: Last glacial and Holocene stable isotope record of fossil dripwater from subtropical



- 835 Brazil based on analysis of fluid inclusions in stalagmites, *Chem. Geol.*, 468, 84–96,
836 doi:10.1016/j.chemgeo.2017.08.018, 2017.
- 837 Moore, P. D., Webb, J. A. and Collinson, M. E.: Pollen analysis, 2ed ed., Blackwell Scientific, Oxford,
838 1991.
- 839 Moser, G., Steindorf, A. and Lange-Bertalot, H.: Neukaledonien Diatomeenflora einer Tropeninsel.
840 Revision der Collection Maillard und Untersuchung neuen Materials., *Bibliotheca Diatomologia*, 32,
841 1–340, 1995.
- 842 Naafs, B. D. A., Inglis, G. N., Zheng, Y., Amesbury, M. J., Biester, H., Bindler, R., Blewett, J.,
843 Burrows, M. A., Torres, D. del C., Chambers, F. M., Cohen, A. D., Evershed, R. P., Feakins, S. J.,
844 Galka, M., Gallego-Sala, A., Gandois, L., Gray, D. M., Hatcher, P. G., Coronado, E. N. H., Hughes, P.
845 D. M., Huguet, A., Könönen, M., Laggoun-Défarge, F., Lähteenoja, O., Lamentowicz, M., Marchant,
846 R., McClymont, E., Pontevedra-Pombal, X., Ponton, C., Pourmand, A., Rizzuti, A. M., Rochefort, L.,
847 Schellekens, J., Vleeschouwer, F. D. and Pancost, R. D.: Introducing global peat-specific temperature
848 and pH calibrations based on brGDGT bacterial lipids, *Goechim. Cosmochim. Ac.*, 208, 285–301,
849 doi:10.1016/j.gca.2017.01.038, 2017.
- 850 Nesbitt, H. W. and Young, G. M.: Early Proterozoic climate and plate motions inferred from major
851 element chemistry of lutites, *Nature*, 299, 715–717, 1982.
- 852 Pearson, E. J., Juggins, S., Talbot, H. M., Weckström, J., Rosén, P., Ryves, D. B., Roberts, S. J. and
853 Schmidt, R.: A lacustrine GDGT-temperature calibration from the Scandinavian Arctic to Antarctic:
854 Renewed potential for the application of GDGT-paleothermometry in lakes, *Geochim. Cosmochim.*
855 *Ac.*, 75, 6225–6238, doi:10.1016/j.gca.2011.07.042, 2011.
- 856 Pedro, J. B., Martin, T., Steig, E. J., Jochum, M., Park, W. and Rasmussen, S. O.: Southern Ocean deep
857 convection as a driver of Antarctic warming events, *Geophys. Res. Lett.*, 43, 2016GL067861,
858 doi:10.1002/2016GL067861, 2016.
- 859 Pedro, J. B., Jochum, M., Buizert, C., He, F., Barker, S. and Rasmussen, S. O.: Beyond the bipolar
860 seesaw: Toward a process understanding of interhemispheric coupling, *Quaternary Sci. Rev.*, 192, 27–
861 46, doi:10.1016/j.quascirev.2018.05.005, 2018.
- 862 Ryan, P.: Field guide to the animals and plants of Tristan da Cunha and Gough Island, Pisces
863 publications, Newbury., 2007.
- 864 Saunders, K. M., Roberts, S. J., Perren, B., Butz, C., Sime, L., Davies, S., Van Nieuwenhuyze, W.,
865 Grosjean, M. and Hodgson, D. A.: Holocene dynamics of the Southern Hemisphere westerly winds
866 and possible links to CO₂ outgassing, *Nat. Geosci.*, 11(9), 650–655, doi:10.1038/s41561-018-0186-5,
867 2018.
- 868 Sime, L. C., Kohfeld, K. E., Le Quéré, C., Wolff, E. W., de Boer, A. M., Graham, R. M. and Bopp, L.:
869 Southern Hemisphere westerly wind changes during the Last Glacial Maximum: model-data
870 comparison, *Quaternary Sci. Rev.*, 64, 104–120, doi:10.1016/j.quascirev.2012.12.008, 2013.
- 871 Sime, L. C., Hodgson, D., Bracegirdle, T. J., Allen, C., Perren, B., Roberts, S. and de Boer, A. M.: Sea
872 ice led to poleward-shifted winds at the Last Glacial Maximum: the influence of state dependency on
873 CMIP5 and PMIP3 models, *Clim. Past*, 12, 2241–2253, doi:10.5194/cp-12-2241-2016, 2016.
- 874 Sjolte, J., Sturm, C., Adolphi, F., Vinther, B. M., Werner, M., Lohmann, G. and Muscheler, R.: Solar
875 and volcanic forcing of North Atlantic climate inferred from a process-based reconstruction, *Clim.*
876 *Past*, 14, 1179–1194, https://doi.org/10.5194/cp-14-1179-2018, 2018.



- 877 Stenni, B., Masson-Delmotte, V., Selmo, E., Oerter, H., Meyer, H., Röthlisberger, R., Jouzel, J.,
878 Cattani, O., Falourd, S., Fischer, H., Hoffman, G., Iacumin, P., Johnsen, S. J., Minster, B. and Udisti,
879 R.: The deuterium excess records of EPICA Dome C and Dronning Maud Land ice cores (East
880 Antarctica), *Quaternary Science Reviews*, 29, 146–159, doi:Stenni, B.; Masson-Delmotte, V.; Selmo,
881 E.; Oerter, H.; Meyer, H.; Röthlisberger, R.; Jouzel, J.; Cattani, O.; Falourd, S.; Fischer, H.; Hoffman,
882 G.; Iacumin, P.; Johnsen, S.J.; Minster, B.; Udisti, R.. 2010 The deuterium excess records of EPICA
883 Dome C and Dronning Maud Land ice cores (East Antarctica). *Quaternary Sci. Rev.*, 29. 146-159.
884 <https://doi.org/10.1016/j.quascirev.2009.10.009> <<https://doi.org/10.1016/j.quascirev.2009.10.009>>,
885 2010.
- 886 Stocker, T. F. and Johnsen, S. J.: A minimum thermodynamic model for the bipolar seesaw,
887 *Paleoceanography*, 18, PA000920, doi:200310.1029/2003PA000920, 2003.
- 888 Tierney, J. E. and deMenocal, P. B.: Abrupt Shifts in Horn of Africa Hydroclimate Since the Last
889 Glacial Maximum, *Science*, 342, 843–846, doi:10.1126/science.1240411, 2013.
- 890 Toggweiler, J. R. and Lea, D. W.: Temperature differences between the hemispheres and ice age
891 climate variability, *Paleoceanography*, 25, PA2212, doi:10.1029/2009PA001758, 2010.
- 892 Toggweiler, J. R., Russell, J. L. and Carson, S. R.: Midlatitude westerlies, atmospheric CO₂, and
893 climate change during the ice ages, *Paleoceanography*, 21, PA2005, doi:200610.1029/2005PA001154,
894 2006.
- 895 Van de Vijver, B., Beyens, L. and Lange-Bertalot, H.: Freshwater diatoms from Ile de la Possession
896 (Crozet Archipelago, Subantarctic), J. Cramer, Berlin., 2002.
- 897 Veres, D., Bazin, L., Landais, A., Toyé Mahamadou Kele, H., Lemieux-Dudon, B., Parrenin, F.,
898 Martinerie, P., Blayo, E., Blunier, T., Capron, E., Chappellaz, J., Rasmussen, S. O., Severi, M.,
899 Svensson, A., Vinther, B. and Wolff, E. W.: The Antarctic ice core chronology (AICC2012): an
900 optimized multi-parameter and multi-site dating approach for the last 120 thousand years, *Clim. Past*,
901 9, 1733–1748, doi:10.5194/cp-9-1733-2013, 2013.
- 902 Waelbroeck, C., Labeyrie, L., Michel, E., Duplessy, J. C., McManus, J. F., Lambeck, K., Balbon, E.
903 and Labracherie, M.: Sea-level and deep water temperature changes derived from benthic foraminifera
904 isotopic records, *Quaternary Sci. Rev.*, 21, 295–305, doi:10.1016/S0277-3791(01)00101-9, 2002.
- 905 WAIS Divide Project Members: Precise inter-polar phasing of abrupt climate change during the last ice
906 age, *Nature*, 520, 661–665, doi:10.1038/nature14401, 2015.
- 907 Weber, M. E., Clark, P. U., Kuhn, G., Timmermann, A., Spreng, D., Gladstone, R., Zhang, X.,
908 Lohmann, G., Menviel, L., Chikamoto, M. O., Friedrich, T. and Ohlwein, C.: Millennial-scale
909 variability in Antarctic ice-sheet discharge during the last deglaciation, *Nature*, 510, 134,
910 doi:10.1038/nature13397, 2014.
- 911 Weijers, J. W. H., Schefuss, E., Schouten, S. and Damste, J. S. S.: Coupled Thermal and Hydrological
912 Evolution of Tropical Africa over the Last Deglaciation, *Science*, 315, 1701–1704,
913 doi:10.1126/science.1138131, 2007.
- 914 Werner, M., Haese, B., Xu, X., Zhang, X., Butzin, M. and Lohmann, G.: Glacial–interglacial changes
915 in H₂18O, HDO and deuterium excess – results from the fully coupled ECHAM5/MPI-OM Earth
916 system model, *Geosci. Model Dev.*, 9, 647–670, doi:10.5194/gmd-9-647-2016, 2016.
- 917 Yamoah, K. A., Chabangborn, A., Chawchai, S., Schenk, F., Wohlfarth, B. and Smittenberg, R. H.: A
918 2000-year leaf wax-based hydrogen isotope record from Southeast Asia suggests low frequency
919 ENSO-like teleconnections on a centennial timescale, *Quaternary Sci. Rev.*, 148, 44–53, 2016.



- 920 Zhu, C., Lipp, J. S., Wörmer, L., Becker, K. B., Schröder, J. M. and Hinrichs, K.-U.: Comprehensive
921 glycerol ether lipid fingerprints through a novel reversed phase liquid chromatography–mass
922 spectrometry protocol, *Org. Geochem.*, 65, 53–62, doi:10.1016/j.orggeochem.2013.09.012, 2013.